

Role of Hydrodynamic Cavitation in Fine Particle Flotation

by

Haipeng Li

A thesis submitted in partial fulfillment of the requirements for the degree of

Master of Science

in

Chemical Engineering

Department of Chemical and Materials Engineering
University of Alberta

© Haipeng Li, 2014

Abstract

In this study, the criteria for both homogeneous and heterogeneous nucleation induced by hydrodynamic cavitation were investigated. The interaction of micron size bubbles with fine coal and the effects of the presence of micron size bubbles and bubble aging on bubble and fine coal attachment were examined using a model system. Furthermore, heterogeneous nucleation was investigated as a function of the hydrophobicity of the solid surface.

A novel cavitation tube and a flow visualization cell allowed for studying homogeneous and heterogeneous nucleation by hydrodynamic cavitation in de-ionized (DI) water system, which showed the generation of micron size bubbles when the throat velocity exceeded 8 m/s. It was found that the increase in fluid velocity slightly decreased bubble size, but increased the number of bubbles. Increasing the dissolved gas content led to the decrease in the on-set velocity for both homogeneous and heterogeneous nucleation. Additionally, it was verified that micron size bubbles were able to collide with and aggregate hydrophobic fine coal. The presence of micron size bubbles on the particle surfaces dramatically enhanced the conventional bubbles to attach to them. However, bubble aging was found to be detrimental to the bubble/particle attachment. Finally, it was found that heterogeneous nucleation only occurred on the crevices of the hydrophobic surfaces.

ACKNOWLEDGEMENT

I would like to express my deep gratitude to Professor Zhenghe Xu and Professor Qingxia (Chad) Liu, my supervisors, for their patient guidance, and enthusiastic encouragement.

I would also like to thank Mr. Artin Afacan for his constant help throughout my research, and Dr. David Harbottle for his valuable advice. Special thanks should be given to technicians, Mr. Jim Skwarok, Ms. Jie Ru, Mr. Jason Dibbs, and Mr. Bicknell Clark who constantly provided me valuable information and the instrument trainings. Without their involvement, my work could not be completed.

My appreciation also goes to Ms. Chendi Wu who gave me a good start on the project. My grateful thanks are also extended to Mr. Runzhe Liu whose suggestions and efforts greatly accelerate the project progress.

I appreciate the support and encouragement from fellow group members of the Oil Sands Engineering Research Chair Group. Special thanks should be given to Dr. Louxiang Wang, Dr. Yang Fan, Dr. He Lin, and Ms. Meghan Carrant for their constructive suggestions. I also profoundly appreciate the support and encouragement from the whole members of the Canadian Centre for Clean Coal/Carbon and Mineral Processing Technologies C₅MPT).

I would like to express my great appreciation to financial support from NSERC-CAMIRO Grant on Fine Particle Flotation and NSERC Industrial Research Chair in Oil Sands Engineering, which made this work possible. Finally, I wish to thank my Mom (Xiaoyan Cui), Dad (Nanyan Li) and girlfriend (Shiqing Wang) for their encouragement. I really owe them a lot.

Table of Contents

| | |
|--|----|
| Chapter 1 Introduction | 1 |
| 1.1 Background | 1 |
| 1.2 Thesis objectives | 12 |
| 1.3 Organization of the thesis | 13 |
| Chapter 2 Literature Review | 14 |
| 2.1 Fine particle flotation | 14 |
| 2.2 Homogeneous and heterogeneous nucleation | 16 |
| 2.3 Design of bubble generator | 22 |
| 2.4 Bubble characterization | 23 |
| 2.5 Frothers | 24 |
| Chapter 3 Experimental Setup and Procedures | 27 |
| 3.1 Experimental setup | 27 |
| 3.2 Materials | 29 |
| 3.3 Experimental procedures | 30 |
| 3.3.1 Homogeneous nucleation | 31 |
| 3.3.2 Image analysis method | 31 |
| 3.3.3 FBRM measurement | 32 |
| 3.3.4 Model system used for flotation study | 36 |
| <i>Fine coal preparation</i> | 37 |
| <i>Procedures of model system flotation</i> | 38 |
| <i>Coal oxidation</i> | 39 |
| 3.3.5 Induction timer | 40 |

| | | |
|---|---|-----------|
| 3.3.6 | Degassing and CO ₂ saturation | 42 |
| 3.3.7 | Observation of heterogeneous nucleation | 43 |
| 3.3.8 | Preparation of silicon wafers, galena and sphalerite surfaces | 44 |
| Chapter 4 Results and Discussion | | 46 |
| 4.1 | Effect of fluid velocity on homogeneous nucleation | 46 |
| 4.2 | Effect of dissolved gas content on homogeneous nucleation | 49 |
| 4.3 | Effect of frother addition on homogeneous nucleation | 52 |
| 4.4 | Effect of bubble number density on flotation recovery | 54 |
| 4.5 | Effect of dissolved gas content on flotation recovery..... | 57 |
| 4.6 | Effect of external entrained air on flotation recovery..... | 60 |
| 4.7 | Effect of hydrophobicity on flotation recovery | 61 |
| 4.8 | Effect of fine particle concentration on flotation recovery..... | 63 |
| 4.9 | Effects of micron size bubbles and bubble aging on bubble/solid attachment | 64 |
| 4.10 | Heterogeneous nucleation | 68 |
| Chapter 5 Conclusions | | 69 |
| Chapter 6 Future Work | | 71 |
| References | | 72 |
| Appendix..... | | 84 |

List of Figures

| | |
|---|----|
| Figure 1-1. Typical relationship between flotation recovery and particle size. This figure is re-plotted according to Feng and Aldrich (1999). | 2 |
| Figure 1-2. Schematic diagram of collision phenomenon. This figure is re-plotted according to Parkinson and Ralston (2011). | 3 |
| Figure 1-3. Bubble rising velocity as a function of bubble diameter. The bubble rising velocity was calculated based on the model proposed by Jamialahmadi et al. (1994). | 6 |
| Figure 1-4. Collision probability as a function of particle size. | 7 |
| Figure 1-5. Schematic diagram of the effect of frosting micron size bubbles on the effective contact angle and bubble/solid contact area (Zhou et al., 2009). | 8 |
| Figure 1-6. Schematic diagram of a venturi style contraction. | 10 |
| Figure 1-7. Schematic diagram of the two-stage aeration concept in flotation. | 11 |
| Figure 2-1. Contact angle correction function, $\varphi(\theta)$ as a function of θ | 19 |
| Figure 3-1. Schematic diagram of the flow circulation loop. | 26 |
| Figure 3-2. Schematic diagram and dimensions of the venturi style cavitation tube. | 27 |
| Figure 3-3. Schematic diagram and dimensions of the visualization cell. | 28 |
| Figure 3-4. Schematic diagram of the FBRM probe. | 31 |
| Figure 3-5. Comparison between bubble size distributions obtained using the FBRM and image analysis methods. | 33 |
| Figure 3-6. Bubble size and chord length as a function of throat velocity. | 34 |
| Figure 3-7. Bubble number counts by FBRM in DI water as a function of throat velocity. | 34 |

| | |
|--|----|
| Figure 3-8. The particle size distribution of fine coal. | 36 |
| Figure 3-9. Contact angle of compressed coal pellet and polished coal chunk..... | 38 |
| Figure 3-10. Photograph of induction timer used in this study. | 39 |
| Figure 3-11. Dissolved CO ₂ content at different dilution ratios..... | 41 |
| Figure 3-12. Contact angle of the silicon wafer before and after DDMS coating..... | 42 |
| Figure 4-1. Bubble diameter distribution as a function of throat velocity. | 44 |
| Figure 4-2. Number mean of chord length, D_{c10} and Sauter mean of chord length, D_{c32} as a function of throat velocity. | 46 |
| Figure 4-3. Number counts of bubbles as a function of throat velocity. | 46 |
| Figure 4-4. The number mean of chord length, D_{c10} and Sauter mean of chord length, D_{c32} as a function of throat velocity. | 47 |
| Figure 4-5. Number counts of bubbles generated in degassed water as a function of throat velocity. | 48 |
| Figure 4-6. Number mean of chord length, D_{c10} and Sauter mean of chord length, D_{c32} as a function of dissolved CO ₂ content at throat velocity of 10.1 m/s..... | 49 |
| Figure 4-7. Number counts of bubbles as a function of the dissolved CO ₂ content at throat velocity of 10.1 m/s. | 50 |
| .Figure 4-8. Effect of 10 ppm MIBC addition on number mean of chord length, D_{c10} and Sauter mean of chord length, D_{c32} as a function of throat velocity. | 51 |
| Figure 4-9. Number counts of bubbles as a function of throat velocity with 10 ppm MIBC addition. | 52 |
| Figure 4-10. Flotation kinetics of fine coal as a function of throat velocity. | 53 |

| | |
|---|----|
| Figure 4-11. Ultimate recovery of fine coal as a function of throat velocity. | 54 |
| Figure 4-12. A typical image of the froth collected in the model fine coal flotation system. | 54 |
| Figure 4-13. Flotation kinetics of fine coal as a function of dissolved CO ₂ content..... | 56 |
| Figure 4-14. Flotation kinetics of fine coal in CO ₂ saturated solution as a function of throat velocity. | 56 |
| Figure 4-15. Ultimate recovery of fine coal in CO ₂ saturated solution as a function of throat velocity. | 57 |
| Figure 4-16. Residual CO ₂ concentration in the solution as a function of flotation time. .. | 57 |
| Figure 4-17. Flotation kinetics of fine coal as a function of time for various amount of external air addition into the cavitation tube. | 58 |
| Figure 4-18. Flotation kinetics of fine coal as a function of coal surface hydrophobicity.. | 59 |
| Figure 4-19. Images of silicon wafers with different contact angles after the collection of micron size bubbles. (a) silicon wafer of $\theta = 62^\circ$; (b) silicon wafer of $\theta = 45^\circ$. The throat velocity was kept constant at 10.1 m/s..... | 60 |
| Figure 4-20. Flotation recovery as a function of time for fine coal slurry of three different concentrations..... | 61 |
| Figure 4-21. Images of induction time experiments with and without micron size bubbles. (a) Silicon wafer without micron size bubbles; (b) silicon wafer frosted with micron size bubbles. | 62 |
| Figure 4-22. Induction time for silicon wafer ($\theta = 65^\circ$) with and without micron size bubbles in DI and Syncrude process water..... | 63 |
| Figure 4-23. Effect of aging micron size bubbles on induction time. | 64 |

| | |
|--|----|
| Figure 4-24. Effect of aging both flotation size and micron size bubbles on induction time. | 64 |
| Figure 4-25. Optical micrographs of (a) silicon; (b) galena; (c) sphalerite surfaces after polishing with 220 grits sand paper. | 66 |
| Figure 4-26. Heterogeneous nucleation on a silicon wafer of contact angle 96° in de- ionized water at throat velocity of 6 m/s. | 68 |

List of Tables

| | |
|--|----|
| Table 1. Composition of the Syncrude process water (ppm). | 29 |
| Table 2. Summary of the observations of heterogeneous nucleation. | 67 |

NOMENCLATURE

| | |
|--------------|--|
| A_1 | cross section area of approach pipe |
| A_2 | cross section area at the contraction |
| D_b | particle diameter |
| D_{cor} | bubble diameter after correction |
| D_{C10} | number mean of chord length |
| D_{C32} | Sauter mean of chord length |
| D_{dec} | detected bubble diameter |
| D_p | particle diameter |
| C_A | gas concentration in gas phase |
| C_W | gas concentration in liquid phase |
| D_{10} | number mean diameter |
| D_{32} | Sauter mean diameter |
| F | gas flux across the air/water interface |
| g | gravitational acceleration |
| h_L | head loss |
| P | total collection probability |
| P_1 | local pressure at the approach pipe |
| P_2 | local pressure at the contraction |
| P_a | attachment probability |
| P_c | collision probability |
| P_d | detachment probability |
| P_v | vapor pressure |
| P_∞ | fluid pressure at the upstream |
| u_b | terminal bubble rising velocity |
| S | super-saturation ratio |
| μ_l | liquid viscosity |
| u_{sb} | terminal bubble rising velocity |
| u_w | terminal bubble rising velocity out of the Stokes region |
| V_{throat} | average throat velocity |
| V_1 | fluid local velocity in the approach pipe |

| | |
|-------------------|--|
| V_2 | fluid velocity at the contraction |
| V_∞ | fluid velocity at the upstream |
| Re_b | bubble Reynolds number |
| ΔG_H^* | minimum Gibbs energy for gas nucleation on solid |
| ΔG^* | minimum Gibbs free energy for gas nucleation |
| ΔG_v | Gibbs free energy of unit volume gas |
| α | Ostwald solubility coefficient |
| α_{cor} | correction coefficient |
| θ | contact angle |
| ρ_g | gas phase density |
| ρ_l | liquid phase density |
| σ | surface tension of fluid |
| σ_n | cavitation number |
| $\varphi(\theta)$ | contact angle correction function |

ABBREVIATIONS

| | |
|-------------|--------------------------------------|
| CCC | critical coalescence concentration |
| CFD | computational fluid dynamics |
| DAF | dissolved air flotation |
| DDMS | dichlorodimethylsilane |
| DI | de-ionized |
| FBRM | focused beam reflectance measurement |
| PAX | potassium amyl xanthate |
| MIBC | methyl isobutyl carbinol |
| TCA | total carbon analyzer |

Chapter 1

Introduction

1.1 Background

Froth flotation is based on surface wettability to recover or remove the target minerals from a multiple phase system. Froth flotation has been extensively used in mineral extraction and waste treatment industries for over 100 years (Anfruns and Kitchener, 1977; Yoon and Luttrell, 1986; Yap et al., 2005). Due to the hydrophobic driving force between hydrophobic particles and gas bubbles (Yoon et al., 1997), the gas bubbles preferentially attach to hydrophobic particles, and form bubble/particle aggregates. As long as the overall density of the bubble/particle aggregates is less than the medium density, the bubble/particle aggregates would float by buoyancy force, and gradually form a froth layer on the top of the flotation cell or flotation column. On the other hand, the hydrophilic particles will not be able to attach to the gas bubbles, rejecting from the bottom of flotation cell or column as tailings. In this way, different kinds of particles can be separated based on their wettability.

Many researchers have shown that the flotation recovery is dependent on the particle size. A typical relationship between flotation recovery and particle size is shown in Figure 1-1. For conventional flotation, good recovery can be obtained when the particle size is in the range of 50 μm to 250 μm (Tao, 2004). The performance of conventional flotation deteriorates rapidly as particle size decreases from 50 μm to fine particles of $\sim 10 \mu\text{m}$ (Feng and Aldrich, 1999). To date, the fine particle flotation is still considered as a challenge in

mineral processing. However, the rapid depletion of high grade ores forces mineral industry to process low grade ores where finer grinding is required to achieve required liberation of the values, making the fine particle flotation necessary. Thus, exploring efficient ways to enhance fine particle flotation has both great economic and scientific values.

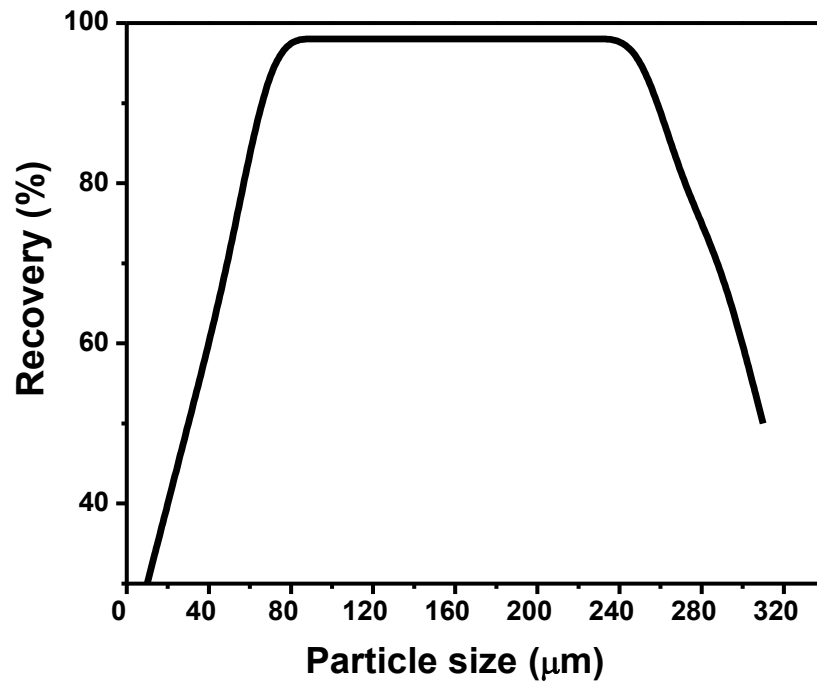


Figure 1-1. Typical relationship between flotation recovery and particle size. This figure is re-plotted according to Feng and Aldrich (1999).

Generally, the whole flotation process is determined by three distinct sub-processes: collision, attachment, and detachment. The total collection probability P could be expressed as (Yoon and Luttrell 1986):

$$P = P_c P_a (1 - P_d) \quad (1.1)$$

where P_c is the bubble/particle collision probability; P_a is the bubble/particle attachment probability; P_d is the bubble/particle detachment probability. Equation (1.1) shows that total collection probability increases with the increase in the bubble/particle collision and attachment probabilities, and decreases with the increase in the detachment probability.

Many researchers established flotation models to investigate the cause of the low recovery of fine particle flotation (Trahar and Warren, 1976; Tao et al., 2004; Yoon and Luttrell, 1986). Although their modeling procedures were different, they made a same conclusion that the decrease in particle size reduces the bubble/particle collision probability. The insufficient bubble/particle collision probability accounts for the low recovery of fine particle flotation. To illustrate, the collision phenomenon between a bubble and a particle is shown in Figure 1-2 (Derjaguin and Dukhin, 1993; Parkinson and Ralston, 2011).

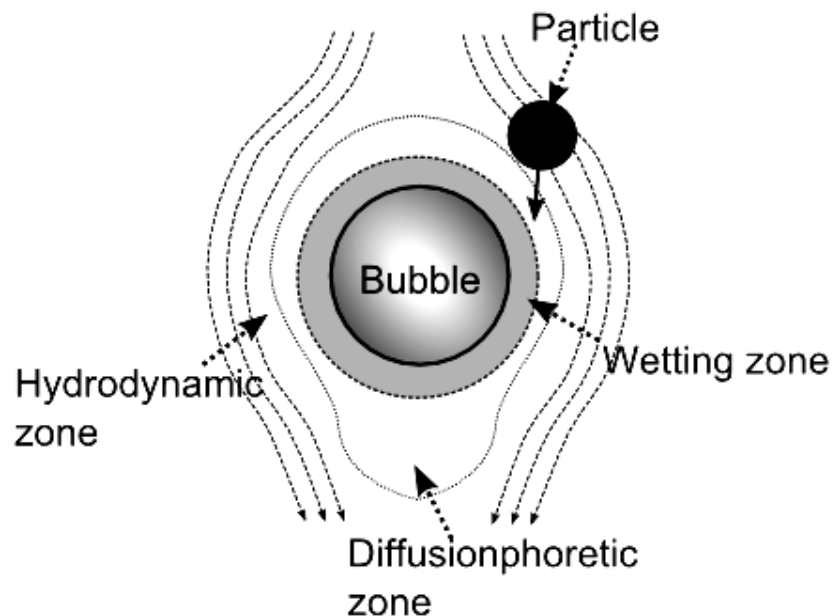


Figure 1-2. Schematic diagram of collision phenomenon. This figure is re-plotted according to Parkinson and Ralston (2011).

Parkinson and Ralston (2011) stated that a successful collision process required the approaching particle to penetrate through three influential zones around a rising bubble in sequence. The most outer zone, normally referred to as hydrodynamic zone, is the layer where the trajectory of the approaching particle is determined by hydrodynamic forces; the zone in the middle is normally called diffusionphoretic zone. The dominate forces in this zone are from electrical field gradient caused by the imbalanced ions during bubble rising; the most inner zone is the region where the surface forces between the bubble and particle are dominating. Compared to medium or coarse particles, fine particles tend to be excluded from the hydrodynamic zone due to their insufficient inertia. Since the Stokes Number for fine particles ($D_{50} \sim 10 \mu\text{m}$) is less than 1, the fine particles are most likely to follow rather than break the streamline. In other words, without the assistance of high turbulence, the fine particles tend to be pushed away from the flotation size bubbles. To further quantify the effect of the particle size on bubble/particle collision probability, the collision model proposed by Yoon and Luttrell (1986) were used to calculate the collision probability at various bubble and particle sizes:

$$P_c = \frac{3}{2} \left(\frac{D_p}{D_b} \right)^2 \left[1 + \frac{\frac{3}{16} \text{Re}_b}{1 + 0.249 \text{Re}_b^{0.56}} \right] \quad (1.2)$$

where P_c stands for the bubble/particle collision probability; D_p and D_b is the particle and bubble diameter, respectively; The Reynolds number, Re_b is the bubble Reynolds number which can be expressed as:

$$\text{Re}_b = \frac{u_b \rho_l D_b}{\mu_l} \quad (1.3)$$

where u_b is the terminal bubble rising velocity; ρ_l is the liquid density and μ_l stands for the liquid viscosity. The terminal bubble velocity is evaluated based on the model proposed by Jamialahmadi et al. (1994):

$$u_b = \frac{u_{sb} u_w}{\sqrt{u_{sb}^2 + u_w^2}} \quad (1.4)$$

where u_{sb} is the terminal bubble rising velocity inside Stokes region, and u_w is the terminal bubble rising velocity outside of the Stokes region. The expression of u_{sb} and u_w is specified in (1.5) and (1.6), respectively.

$$u_{sb} = \frac{1}{18} \frac{\rho_l - \rho_g}{\mu_l} g D_b^2 \quad (1.5)$$

$$u_w = \sqrt{\frac{2\sigma}{D_b(\rho_l + \rho_g)} + \frac{g D_b}{2}} \quad (1.6)$$

where ρ_g is the density of air; σ represents the surface tension of solution; g is the gravitational acceleration. The model proposed by Jamialahmadi et al. (1994) is selected, since it is verified to be able to predict the rising velocity of bubbles with diameter of 1 μm to 8 cm.

Substituting equations (1.5) and (1.6) into equation (1.4), a bubble/particle collision probability model can be established. Here, the bubble/particle collision probabilities for

particle diameters of 100 μm , 20 μm and 10 μm were calculated and compared. Figure 1-3 shows the calculated bubble rising velocities. Apparently, the bubble rising velocity increases with the increase in diameter. The calculated bubble/particle collision probabilities are shown in Figure 1-4. The results in Figure 1-4 show that the decrease in particle diameter leads to a rapid decrease in bubble/particle collision probability. In conventional flotation, gas bubbles are usually generated by air sparging method. The diameter of bubbles generated by this method ranges from 600 μm to 2000 μm (Tao et al., 2004). In this study, the bubbles generated by air sparging method are referred to as flotation size bubbles. Clearly, collision probability between fine particles ($D_{50} \sim 10 \mu\text{m}$) and flotation size bubbles is less than 5 %, indicating that flotation size bubbles are not suitable for fine particle flotation. Figure 1-4 also reveals that reducing bubble size is a promising method to enhance the bubble/particle collision probability so as to the flotation recovery.

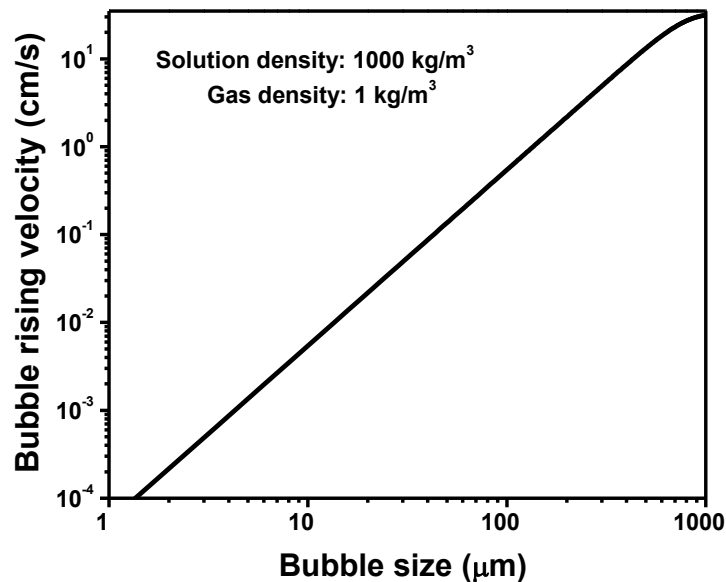


Figure 1-3. Bubble rising velocity as a function of bubble diameter. The bubble rising velocity was calculated based on the model proposed by Jamialahmadi et al. (1994).

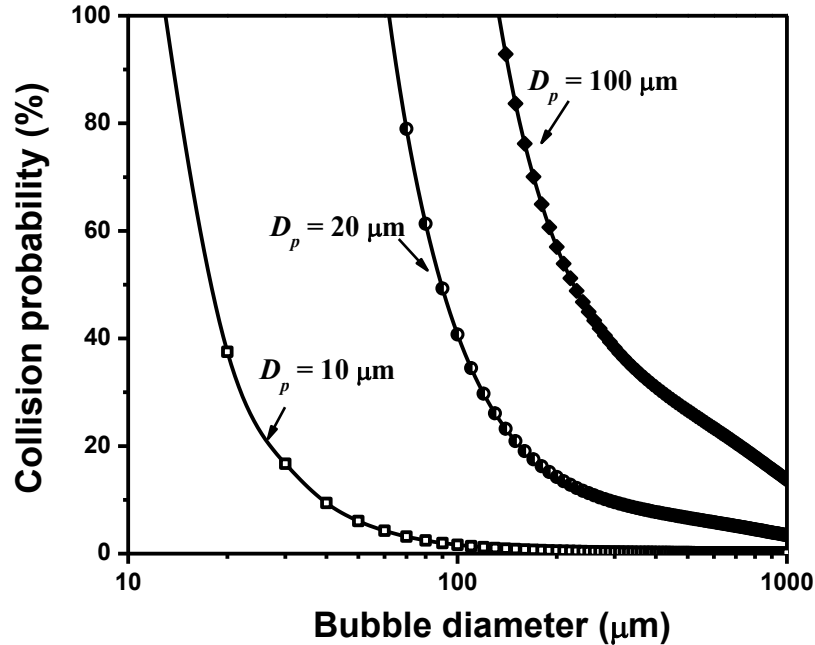


Figure 1-4. Collision probability as a function of particle diameter.

Yoon and Luttrell (1986), Subrahmanyam and Forsberg (1990) pointed out that, besides low bubble/particle collision probability, rapid oxidation, high chemical consumption due to the large surface area of fine particles, high gangue mineral entrainment, etc., are also challenging problems in fine particle flotation.

The introduction of micron size bubbles to conventional flotation cell would benefit the fine particle flotation. First, the presence of micron size bubbles leads to the aggregation of hydrophobic fine particles, which increases bubble/particle collision probability by increasing the inertia of fine particles. Second, the micron size bubbles frosting on the solid surface are expected to increase the bubble/particle attachment probability (Sobhy and Tao, 2013; Zhou et al., 2009). A possible mechanism of the attachment enhancement due to the presence of micron size bubbles proposed by Zhou et al. (2009) is illustrated in Figure 1-5.

The presence of micron size bubbles on a solid surface enhances the attachment probability by increasing the effective contact angle of the solid surface from α to β , as shown in Figure 1-5, and enlarging the bubble/solid contact area.

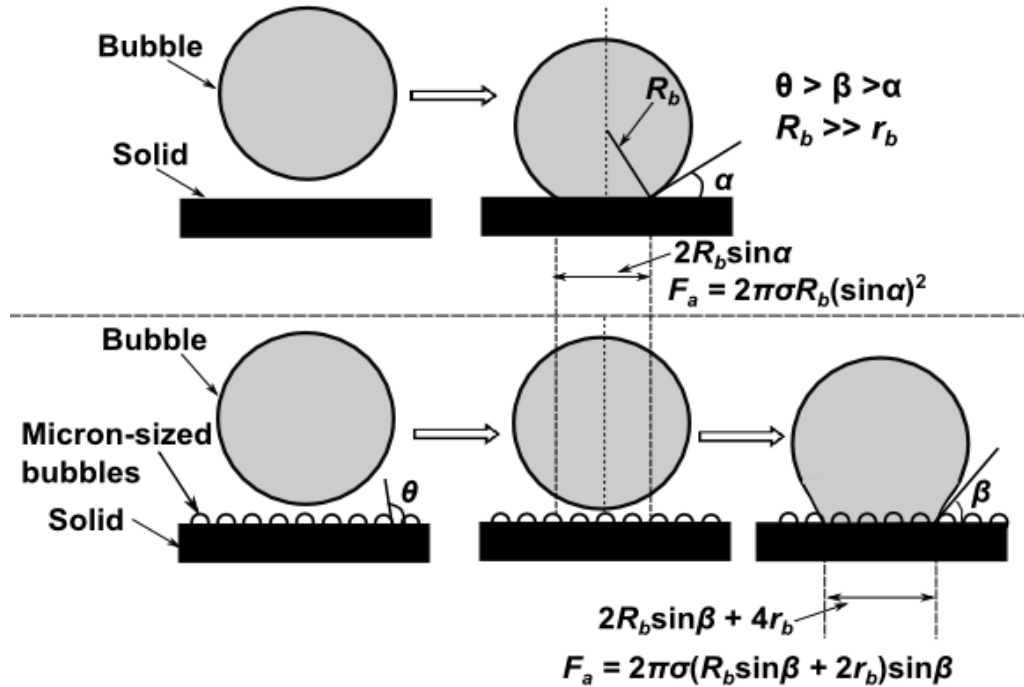


Figure 1-5. Schematic diagram of the effect of frosting micron size bubbles on the effective contact angle and bubble/solid contact area (Zhou et al., 2009).

Previous studies provided us a few options to generate micron size bubbles, such as hydrodynamic cavitation, optical focus, ultrasonic oscillation, electrolysis, etc. (Xu et al., 2008). In practice, the high energy consumption, installation inconvenience and maintenance difficulty encountered in ultrasonic, optical focus and electrolysis methods exclude them from being used in practical flotation operation (Feng and Aldrich, 1999). On the other hand, it is evident that hydrodynamic cavitation is applicable to practical flotation operation. Canadian Process Technologies Inc. (CPT) already recognized the potential of

hydrodynamic cavitation in fine particle flotation, and has successfully commercialized their hydrodynamic cavitation system. CPT conducted a few pilot tests on the cavitation system at several Brazilian phosphate flotation plants. The results from such pilot plant tests showed that hydrodynamic cavitation increased phosphate flotation recovery by 2% ~ 3% on average (ERIEZ 2013). Additionally, laboratory tests reported by Tao et al. (2008) and Sobhy and Tao (2013) confirmed that hydrodynamic cavitation could enhance the fine particle flotation recovery. Therefore, hydrodynamic cavitation is considered as a viable method to enhance the flotation recovery. That is the reason why the effect of hydrodynamic cavitation on the flotation of fine particles is the subject of this study.

In this study, hydrodynamic cavitation is specifically referred to as the creation of gas nuclei through pressure reduction achieved by increasing the fluid velocity. The fundamental principle of hydrodynamic cavitation could be described by Bernoulli equation across any contractions:

$$\frac{P_1}{\rho} + \frac{V_1^2}{2} = \frac{P_2}{\rho} + \frac{V_2^2}{2} = h_L \quad (1.7)$$

where P_1 and P_2 represent the local pressure at point 1 and point 2, respectively; V_1 and V_2 stand for the fluid velocities in the approach pipe, and at the contraction and h_L is the head loss. Figure 1-5 shows venturi style contraction. By modifying the ratio of the inlet cross section area, A_1 to the cross section area of the contraction, A_2 (i. e., A_1/A_2), the local fluid velocity can be controlled. The increase in the fluid velocity results in the reduction in local pressure. When the local pressure is reduced under a critical point, hydrodynamic cavitation occurs.

In practice, the wall effect would make the hydrodynamic cavitation preferentially occur in the vicinity of the walls, which has been conceptually shown in Figure 1-6. Athavale et al. (2002) reported that the wall enhanced the hydrodynamic cavitation by strengthening the local turbulence. As well known, stronger turbulence leads to faster energy dissipation, which benefits hydrodynamic cavitation.

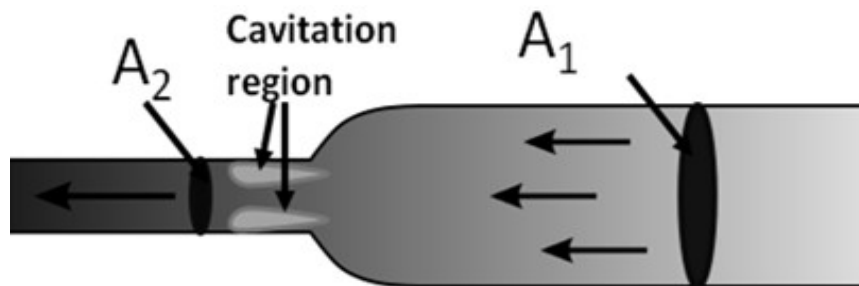


Figure 1-6. Schematic diagram of a venturi style contraction.

However, the micron size bubbles cannot provide sufficient buoyancy force to float mineral particles, especially coarse particles. Thus, the involvement of flotation size bubbles is still required. Therefore, it is suggested that the micron size bubbles should be introduced into flotation cells as a complement rather than an alternative of flotation size bubbles, giving birth to the concept of two-stage aeration (Nesset et al., 2006; Tao et al., 2006; Zhou et al., 2010). A schematic diagram of the two-stage aeration concept in flotation is illustrated in Figure 1-7. In the first stage, micron size bubbles generated by hydrodynamic cavitation frost on the surfaces of particles. The micron size bubbles on the fine particle surfaces could lead to the aggregation of fine particles (Wei et al., 2009; Wu, 2011), which enhances the collection probability between fine particles and flotation size bubbles. In the second stage, flotation size bubbles attach to the aggregates of fine particles

and bring them to the top of the slurry. Since the surfaces of fine particle aggregates are frosted with micron size bubbles, the attachment between flotation size bubbles and fine particle aggregates is stronger than direct attachment between flotation size bubbles and fine particles.

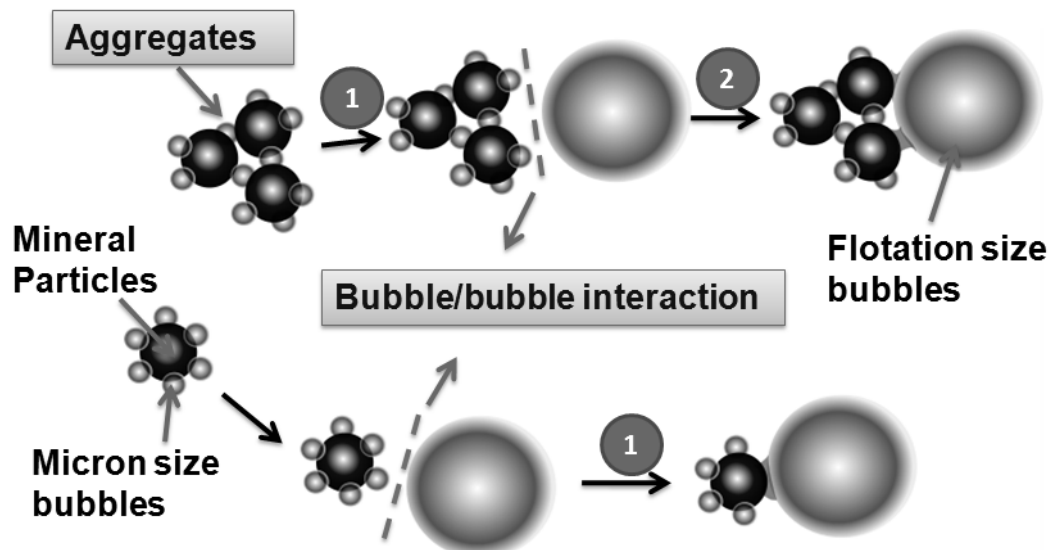


Figure 1-7. Schematic diagram of the two-stage aeration concept in flotation.

1.2 Thesis objectives

The main objective of this thesis research is to investigate the role of hydrodynamic cavitation in fine particle flotation. The effect of fluid velocity, dissolved gas content, and addition of frother on the hydrodynamic cavitation in air/water (homogenous nucleation) system and the interaction between micron size bubbles and fine particles was investigated. In addition, the effect of the presence of micron size bubbles and bubble aging on the attachment between flotation size bubble and solid surface was studied. Finally, the preliminary study of heterogeneous nucleation at the solid/liquid

interface was conducted in an in-house made fluid visualization chamber to understand the effect of fluid velocity and dissolved gas content on heterogeneous nucleation.

1.3 Organization of the thesis

In chapter 1, the fine particle flotation and hydrodynamic cavitation are introduced. In chapter 2, the key issues, such as the fine particle flotation, the definitions of homogeneous and heterogeneous nucleation, design of bubble generator, bubble characterization techniques, and the functions of frother in bubble generation, are reviewed. In chapter 3, the experimental apparatuses and procedures for the investigation of homogeneous and heterogeneous nucleation, model system used for flotation study, and bubble/solid attachment are specified. In chapter 4, the experimental results are reported and discussed. In chapter 5, the results obtained are summarized. In chapter 6, future work regarding the hydrodynamic cavitation in fine particle flotation is proposed. Through this study, the criteria for the hydrodynamic cavitation in liquid bulk (homogeneous nucleation) and at the solid/liquid interface (heterogeneous nucleation) will be established. In addition, the interaction between micron size bubbles and fine particles will be investigated using model system for flotation tests and induction time measurement. The knowledge obtained in this study is intended to guide the design of the novel bubble generator for fine particle flotation.

Chapter 2

Literature Review

2.1 Fine particle flotation

According to Subrahmanyam and Forsberg (1990), the fine particle flotation is defined as the recovery of particles with diameter of 5 - 20 μm . As demonstrated, the recovery of fine particle is relatively low even when the dosages of collector and frother have been optimized (Trahar and Warren, 1976). Many methods have been developed with the attempt to increase the recovery of fine particle flotation. These methods include oil flotation, flocculation flotation, shear flocculation flotation, carrier flotation, dissolved air flotation (DAF) and hydrodynamic cavitation assisted flotation (Trahar and Warren, 1976; Dianzuo et al., 1988; Tao et al., 2006; Rodrigues and Rubio, 2007; Zhou et al., 2010; Zhou et al., 2013). For oil flotation and flocculation methods, chemicals are added to aggregate fine particles. Particle aggregation increases the overall particle size, which results in an increase in bubble/particle collision. It is found that aggregation only occurs when the dosage of the oil or chemical added exceeds a certain threshold value. However, in most cases, the minimum dosage required for particle aggregation is still too high to be applicable to mineral processing from the economic point of view (Parker et al., 1994; Song et al., 2000). Shear flocculation flotation and carrier flotation share some common characters. They both utilize the mechanical forces to directly aggregate the hydrophobic particles. There are two critical requirements for shear flocculation flotation and carrier flotation (Gorain et al., 1997; Song et al., 2001; Piñeres and Barraza, 2011): 1) both fine and carrier particles should be hydrophobic, and 2) intensive agitation is normally required

to obtain sufficient collision among fine particles. The behaviors of the hydrophobic particle aggregation could be explained by the extended DLVO theory (Boström et al., 2006). And it is found that the dosage of collector, pH value, and agitation condition profoundly affect the performance of shear flocculation flotation and carrier flotation (Xu and Yoon, 1989; Lu et al., 1998). The shortcoming of shear flocculation flotation and carrier flotation is that hydrophilic particles are frequently trapped in the hydrophobic aggregates, which is detrimental to the selectivity of flotation (Rodrigues and Rubio, 2007).

The dissolved gas flotation (DAF) and hydrodynamic cavitation assisted flotation belong to the third category – gas nucleation method. In both methods, fine bubbles (<100 µm) are injected into the flotation cell to enhance the flotation recovery. And the fine bubbles are generated through pressure reduction. The DAF is widely used in water purification (Collins and Read, 1971; Finch and Hardie, 1999; Oliveira et al., 1999; Féris et al., 2001). Recent studies show that the DAF has the potential of being used in mineral separation (Lazaridis et al., 1993; Rodrigues and Rubio, 2007). However, it is difficult to control the bubble generation rate in DAF. A sudden swarm of bubbles are normally presented at the pressure releasing moment. Consequently, gangue mineral entrainment is a serious concern in DAF. The hydrodynamic cavitation assisted flotation is based on the reduction of the pressure by increasing the fluid velocity. Zhou et al. (1997) and Wu (2011) suggested that the bubble generation rate during hydrodynamic cavitation can be controlled by fluid velocity. With such approach, the problem of gangue mineral entrainment in DFA would not occur or can be controlled in hydrodynamic cavitation assisted flotation (Sobhy and Tao, 2013). To test the performance of hydrodynamic cavitation assisted flotation, Zhou et al. (1997) constructed their own cavitation reactor, and mounted it on a batch flotation cell.

They found that the recovery of 1 % (w/w) silica with addition of 0.125 mM dodecyl amine was increased from 30% to ~ 33% when hydrodynamic cavitation was integrated. Similar results were reported by Yu et al. (2006), Wei et al. (2009), Zhou et al. (2010) and Sobhy and Tao (2013). Additionally, Tao et al. (2006; 2008) showed that the presence of the micron size bubbles halved the optimum collector dosage. Another observation is that when micron size bubbles were presented, the froth layer became more stable. There is a general agreement about the concept that hydrodynamic cavitation could enhance the fine particle flotation recovery, but the enhancement is only 2-3 % on average. To break the bottleneck, it is important to investigate which parameter limits the performance of the hydrodynamic cavitation assisted flotation.

2.2 Homogeneous and heterogeneous nucleation

According to the Henry's law, the amount of the dissolved gas in solution is proportional to the saturation pressure. In hydrodynamic cavitation, a sudden pressure reduction caused by either agitating or pushing fluid through a narrow contraction makes the solution in a temporary super-saturation state. In super-saturation state, certain amount of the dissolved gas releases from the liquid phase, becoming free gas molecules in the solution. The free gas molecules are seeds of micron size bubbles. The clusters of the free gas molecules further accumulate to form the micron size bubbles. The cluster process is referred to as gas nucleation. The gas nucleation determines the properties of the micron size bubbles generated. According to Bernnen (1995), gas nucleation could be generally classified into two categories: homogeneous nucleation and heterogeneous nucleation. Normally, homogeneous nucleation refers to the nucleation occurring in the interior of a homogenous

phase. In this study, homogenous nucleation specifically refers to the gas nucleation in air/water system; heterogeneous nucleation stands for the gas nucleation at the solid/liquid interface.

The classical gas nucleation theory has been established and extended by several authors over 50 years (Blake, 1949; Sigsbee and Pound, 1967; Motarjemi and Jameson, 1978; Noppel et al., 2013). In the landmark work proposed by Sigsbee and Pound (1967), the main frame of the classical gas nucleation model has been developed. By counting the net volume work of condensation and surface work, the classical gas nucleation theory is able to predict the minimum Gibbs energy required for gas nucleation, ΔG^* . The ΔG^* relates to the Gibbs free energy of unit volume for gas nucleation, ΔG_v , and surface tension, σ by equation (2.1):

$$\Delta G^* = \frac{16}{3} \pi \frac{\sigma^3}{\Delta G_v^2} \quad (2.1)$$

where ΔG_v is expressed as:

$$\Delta G_v = \frac{-kT}{v} \ln S \quad (2.2)$$

where S is the super-saturation ratio. When the input energy is less than ΔG^* , gas nuclei tend to collapse rather than expand to stable bubbles. Equations (2.1) and (2.2) reveal that the input Gibbs energy can be increased by increasing temperature and super-saturation ratio. Gas nucleation generated by increasing temperature refers to as boiling process, while gas nucleation caused by pressure reduction is hydrodynamic cavitation.

For hydrodynamic cavitation, the trends predicted by the classical theory agree well with the experimental observations. The classical theory shows that ΔG^* is inversely proportional to S . This trend has been supported by many experimental studies. Harvey et al. (1947), Blake (1949), Wei et al. (2009) and Zhou et al. (2010) showed that the increase in the dissolved gas content enhanced the gas nucleation rate. On the other hand, the studies by Harvey et al. (1947) and Zhou et al. (1997) showed that degassing which reduced the super-saturation ratio decreased the gas nucleation rate. However, Wily (1986) found that the bubble generation rate evaluated by the classical theory in CO₂ saturated solution was two orders of magnitude lower than the experimental observation.

A few assumptions have been made to fill the gap between classic thermodynamic theory and experimental observation. Brennen (1995) and Tao (2004) proposed that there might be pre-existing cavities in solution, especially for the super-saturated solution. These pre-existing cavities might function as the nucleation sites, and greatly reduce the energy required for gas nucleation. Second, contaminants presented reduce ΔG^* required (Harvey et al., 1947; Brennen, 1995). Third, the intensive vortexes taking place in the high turbulence regions might be another reason for the discrepancy. Computational Fluid Dynamics (CFD) simulation studies from Singhal et al. (2002) and Rooze et al. (2012) showed that gas nucleation rate in high turbulence region is much higher than that at low turbulence locations. Such a finding has been experimentally confirmed by Zhou (1996), Nettet et al. (2006) and Wu et al. (2012). However, the turbulence is difficult to be directly measured. Therefore, the effect of turbulence on the gas nucleation is still difficult to be experimentally quantified.

In flotation, hydrophobic particles are involved in most cases. Therefore, heterogeneous nucleation might take place and play a crucial role in flotation. According to Fletcher (1959), Sigsbee and Pound (1967) and Qian and Ma (2009), the energy barrier for the heterogeneous nucleation is much lower than that of homogeneous nucleation. This means that gas nuclei might directly form on the particle surface. Sigsbee and Pound (1967) proposed that the minimum Gibbs energy required for the formation of a stable gas nucleus on a flat surface could be evaluated by multiplying the minimum Gibbs energy for homogeneous nucleation with a contact angle correction function:

$$\Delta G_H^* = \Delta G^* \times \varphi(\theta) \quad (2.3)$$

where ΔG_H^* is the minimum Gibbs energy required for the gas nucleation on a flat surface; $\varphi(\theta)$ is the contact angle correction function, which is shown as follows:

$$\varphi(\theta) = \frac{(2 - 3 \cos(\pi - \theta) + \cos^3(\pi - \theta))}{4} \quad (2.4)$$

The value of $\varphi(\theta)$ as a function of contact angle is shown in Figure 2-1. Clearly, the increase in contact angle facilitates the gas nucleation on solid surface. This trend has been supported by many experimental reports. Harvey et al. (1947) reported that, dissolved gas preferred to nucleate on the hydrophobic rod. Zhou (1996) examined the coal flotation in CO₂ dissolved water. He reported that gas nucleation only took place on coal sample with contact angle larger than 70°. Song (1999), Warren (1975), Ding et al. (2009) and Song et al. (2012) showed that the gas nuclei on the hydrophobic particle surfaces led to the

flocculation of hydrophobic particles. Therefore, the concept that presence of the hydrophobic particles enhances the gas nucleation rate has been widely accepted.

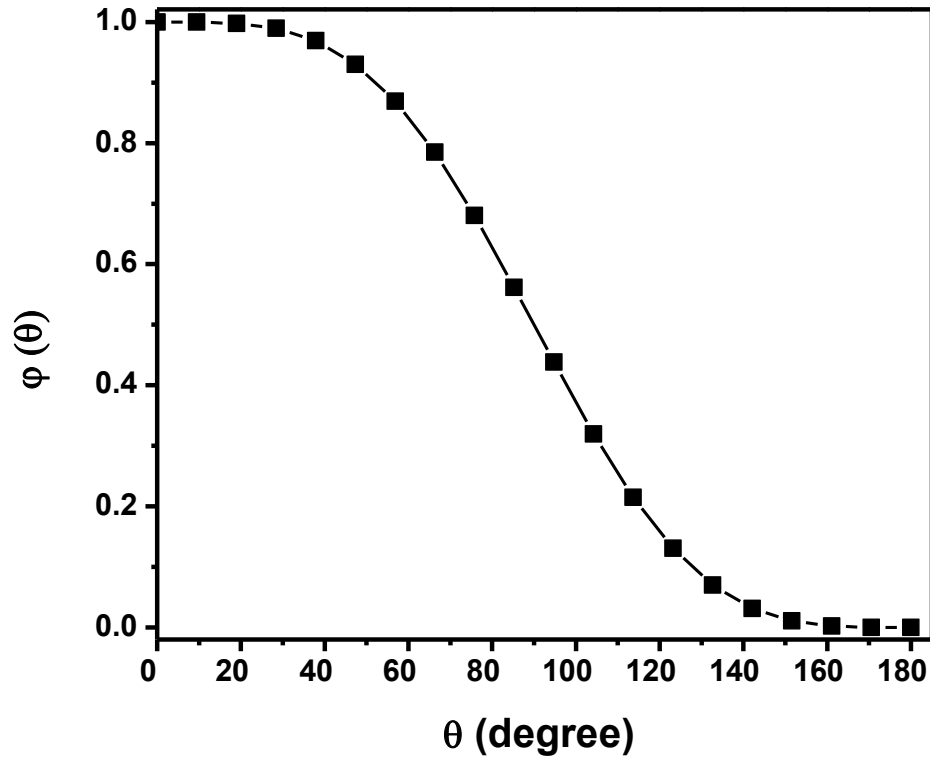


Figure 2-1. Contact angle correction function, $\phi(\theta)$ as a function of θ .

Another actively discussed topic is whether the heterogeneous nucleation observed in flotation requires the presence of the surface roughness. By using the classical nucleation model, Wilt (1986) stated that ΔG^* for the crevices on a solid surface was lower than that on a smooth surface. And he concluded that the crevices on a solid surface served as the nucleation sites for heterogeneous nucleation. To examine the effect of surface roughness on the critical super-heating temperature, Witharana et al. (2012) drilled well controlled holes (diameter: 100 nm - 5 μ m) on a smooth silicon surface. They discovered that as hole diameter was reduced from 5 μ m to 100 nm, the critical heating temperature increased

from 70 °C to 280 °C at atmospheric pressure. In addition, the gas nucleation on smooth hydrophobic Teflon particles was tested by Ryan and Hemmingsen (1993) in N_2 supersaturated solution. They found that even when the saturation pressure went up to 125 atm, no gas nucleation was observed on the smooth hydrophobic surface, suggesting that the energy barrier for gas nucleation on smooth surface was extremely high. Furthermore, Borkent et al. (2008) discovered that the gas nucleation rate on a hydrophobic smooth wafer increased from 0.3 bubbles per mm^2 to 160 bubbles per mm^2 when experimental location was moved out of a clean room. This indicates that the contaminants on a solid surface due to the exposure to the air in a normal lab environment increase heterogeneous nucleation generation rate. Such a conclusion is supported by the molecular dynamics simulation reported by Sear (2006). All of the evidences show that the surface roughness is crucial to the gas nucleation. In flotation, surface roughness and contaminants are inevitable. In most cases, it is difficult to accurately determine the effects of surface roughness of the particles and contaminants on flotation, making the accurate prediction of the role of the hydrodynamic cavitation in flotation still challenging.

Additionally, the reports from molecular dynamics simulation provided additional important information. Ten et al. (1990) discovered that the kinetic pre-factor, a parameter which was proportional to nucleation rate, was ten times larger than the value predicted by classical nucleation theory. Toxvaerd (2002), and Du and Miller (2007) found that a water depletion zone existed near the hydrophobic solid surface, and supersaturated vapor was inclined to concentrate in the water depletion zone. The vapor concentration in the depletion zone might reduce the minimum input energy required for gas nucleation. Zhou et al. (2009) showed that it remained inconclusive whether the heterogeneous nucleation

could occur on surface with contact angles less than 90° . But it has been widely accepted that the fine hydrophobic particles with contact angles from 70° - 90° could enhance the gas nucleation rate by preventing the gas nuclei from re-dissolving into the liquid phase (Brennen, 1995).

2.3 Design of bubble generator

For many decades, the design of bubble generator has always been an actively discussed topic. Xu (2000) summarized that generation of sufficient amount of bubbles with suitable sizes is the basic requirement for a flotation bubble generator. To date, the design of the bubble generator is still highly empirical. The design guidelines are summarised in this section.

Takahashi et al. (1979) investigated the effect of the length of venturi style nozzle on bubble size. Their results showed that increasing the length of a venturi style nozzle enhanced the bubble coalescence, resulting in the increase in bubble size. Ponasse et al. (1998) investigated the effect of the divergence angle of a venturi style cavitation tube on bubble size. They found that larger divergence angle led to a higher degree of turbulence, resulting in a decrease in bubble size. In addition, they also discovered bubble size would be increased if the wall of the cavitation tube was coated by hydrophobic materials. Yan and Thorp (1990) studied the hydrodynamic cavitation in a series of cavitation tubes with increased diameter ratio (the ratio of the diameter of the contraction and the diameter of inlet). This study discovered that diameter ratio had a positive proportional relationship with the inception cavitation number (σ_N). The inception cavitation number (σ_N) is defined in equation (2.5).

$$\sigma_N = \frac{P_\infty - P_v}{\frac{1}{2} \rho_L V_\infty} \quad (2.5)$$

where P_∞ is the fluid pressure at the upstream; P_v is the vapor pressure; V_∞ is the fluid velocity at the upstream. This finding indicated that for cavitation tube with a given diameter, shrinking the cross section area of a contraction facilitated cavitation. Ross and Kuperman (1989) and Zhou (1996) both observed that shorting the tip length and increasing the diameter of a cavitation tube would reduce the number density of bubbles generated.

2.4 Bubble characterization

Many techniques have been developed to analyze the size of bubbles in flotation systems. The image analysis method is the most widely applied technique since its setup and operation are relatively easy. Many research groups, such as Yoon and Luttrell (1986), Tucker et al. (1994), Chen et al. (2001), Grau and Heiskanen (2003), Rodrigues and Rubio (2003) and Nasset et al. (2006) have independently developed their own image analysis setups. The image analysis method was used to be an off-line method. The rapid development of image analysis software and packages is turning image analysis method to be a semi in-situ method. The drawbacks of image analysis methods are also intensively discussed. Inappropriate sampling, de-focus, bubble overlapping, and distortion brought by container deteriorate the measurement accuracy of the image analysis methods. Due to the resolution limitation of optical chips, measuring the bubbles with diameter less than 5 μm is still challenging. In addition to image analysis method, researchers at University of Cap Town successfully measured the size of flotation size bubbles by a capillary bubble size

analyser (Randall et al. 1989; Tucker et al. 1994). This method is normally referred to as UCT method, where bubbles are sucked out of slurry, and forced to pass through a capillary bubble size analyser. For UCT method, sampling accuracy determines the measurement quality. The pilot tests show that the UCT method can be used to determine the flotation size bubbles accurately. However, there is no evidence that this method is applicable to the micron size bubble measurement. It is worth noting that sub micron size bubbles, which could survive in liquid for a couple of hours with the protection from frother, can be counted by ZetaPALS method (Wu et al., 2012). Compared with sub micron size bubbles, micron size bubbles or even larger bubbles have an exponentially shorter residence time in the measurement. So, the ZetaPALS method is not suitable for the measurement of the micron size bubbles.

It can be seen that each method has its own Pros and Cons, and further development is required. Selecting well-suited method to accurately estimate the bubble size is the key to the study of bubble size generation by hydrodynamic cavitation. Commonly, the number based mean diameter, D_{10} , and the Sauter mean diameter, D_{32} , are calculated to evaluate the bubble size. As demonstrated by Nettet et al. (2006), D_{32} is preferred in flotation study, since it correlates with flotation recovery rate more closely.

2.5 Frothers

Frother is a category of surface-active molecules. A typical frother consists of a hydrophilic head and a hydrocarbon chain of minimal length. Adding frothers has profound effect on bubble size, bubble stability, bubble surface properties, and the interaction between bubbles and particles. Melo (2001), Nettet et al. (2006) and Finch et al. (2008)

clearly showed that addition of frothers with concentration lower than their critical coalescence concentration (CCC) led to a quick decrease in bubble size. However, adding frothers with concentration higher than the CCC reduced the bubble size further slowly. Finch et al. (2008) further discovered that, in flotation, bubble size reduction by frother addition was mainly caused by the prevention from bubble coalescence rather than the decrease in surface tension. They also showed that, for a given bubble generator, bubble size almost kept constant if frothers were added at their corresponding CCC. In following sections, methyl isobutyl carbinol (MIBC), an extensively used frother in coal flotation, is used in this study. Finch et al. (2008) reported that the CCC for MIBC was 10 ppm.

It has been noticed for many years that addition of a small amount of frother significantly enhances the stability of bubbles, which could not be explained from the surface tension reduction point of view. Recently, more and more researchers recognized that addition of a small amount of frother greatly enhanced the Gibbs elasticity of the bubble surface which was believed to be the main reason of increased stabilization. The gradient of the surface tension is considered as a more advanced indicator to evaluate the stabilization of bubbles due to the addition of frother.

Addition of appropriate amount of frother is crucial to flotation recovery. First, appropriate addition of frother prevents the bubble coalescence, so as to stabilize the froth layer, which reduces the particle detachment. Second, appropriate addition of frother prevents the bubble deformation, which accelerates the bubble rising velocity. This benefits the collision between bubbles and particles (Clift 2005). Third, Yoon and Jordan (1986) and Wu et al. (2012) reported that addition of frother could change the surface charge of

bubbles. Appropriately manipulating the surface charge of bubbles according to the surface charges of particles in the slurry enhances the bubble/particle attachment.

The literature review above indicates a general lack of an appropriate method to determine the size and number counts of micron size bubbles. To solve the problem, Focused Beam Reflectance Measurement (FBRM), an advanced particle and droplet size measurement technique, will be used to measure the size and number counts of micron size bubbles. Determining the interaction between fine particles and micron size bubbles is another issue that addressed scarcely in open literature. Thus, a model system study will be conducted in the coming sections to investigate the interaction between fine particles and micron size bubbles. Furthermore, we can see that a closer look on heterogeneous nucleation in hydrodynamic cavitation is required to examine the controversy about the criteria of heterogeneous nucleation.

Chapter 3

Experimental Setup and Procedures

3.1 Experimental setup

A flow-loop used to investigate the hydrodynamic cavitation induced homogeneous and heterogeneous nucleations is shown in Figure 3-1. The circulation loop consists of a peristaltic pump (Masterflex, I/P), a cavitation tube and/or a flow visualization cell and a 1600 ml container. Peristaltic pump is used to circulate the solution through either the cavitation tube or the flow visualization cell. The cavitation tube is mainly used for the study of homogeneous nucleation and the generation of micron size bubbles for bubble/particle interaction tests. The flow visualization cell is only used for the investigation of heterogeneous nucleation.

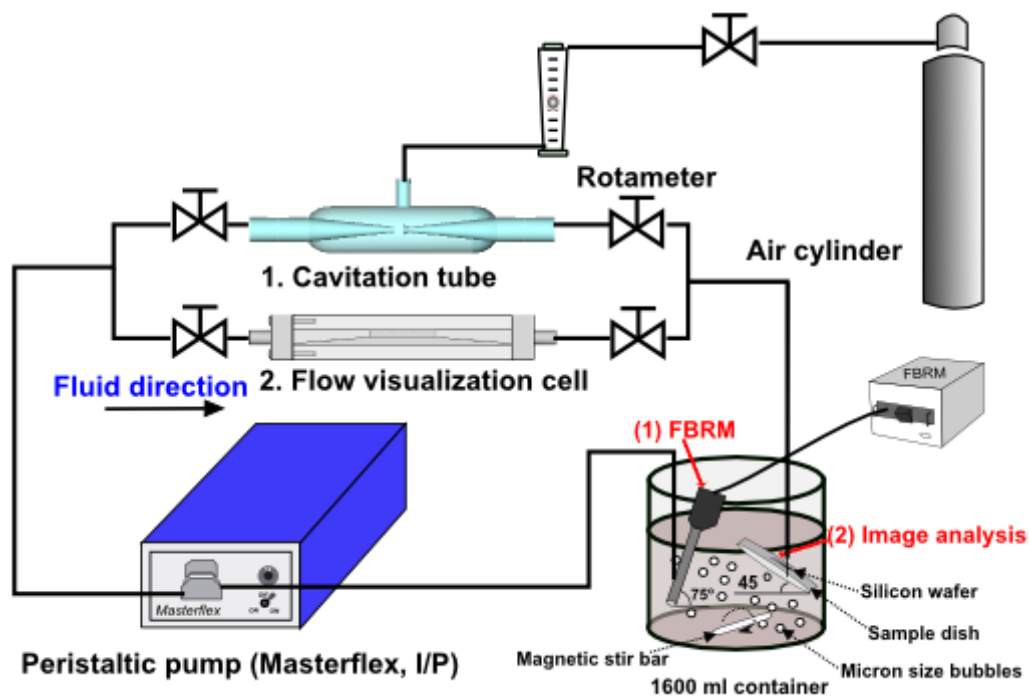


Figure 3-1. Schematic diagram of the flow circulation loop.

The schematics of the cavitation tube and the flow visualization cell are shown in Figures 3-2 and 3-3, respectively. The cavitation tube and flow visualization cell are both venturi style. For venturi style tubes or cells, the flow velocity at the throat regions increases during circulation, reducing the pressure at the throat regions. The micron size bubbles are expected to generate at the throat of the cavitation tube and flow visualization cell when the fluid velocity is sufficient high. The cavitation tube is made of glass. The diameter of the inlet tube is 12.7 mm, and the diameter of the throat of the tube is 2.5 mm, corresponding to a contraction ratio of 0.212 (2.7mm /12.7 mm). Additionally, analytical purity air supplied by a gas cylinder can be injected into the cavitation tube through an air port in the middle of the tube. The air flow rate is measured using a 150 ml/min pre-calibrated rotameter. The flow vislization cell is designed to investigate the heterogeneous nucleation. The flow visulzation cell is made of plexiglass. As shown in Figure 3-3, different kinds of wafers can be mounted on the bottom wall of the visualization cell. The heteogenoues nucleation on the wafter is investigated under an optical microscope (DP72, Olympus). To eliminate the curvature effect, the walls of the visualization cell are constructed in square shape.

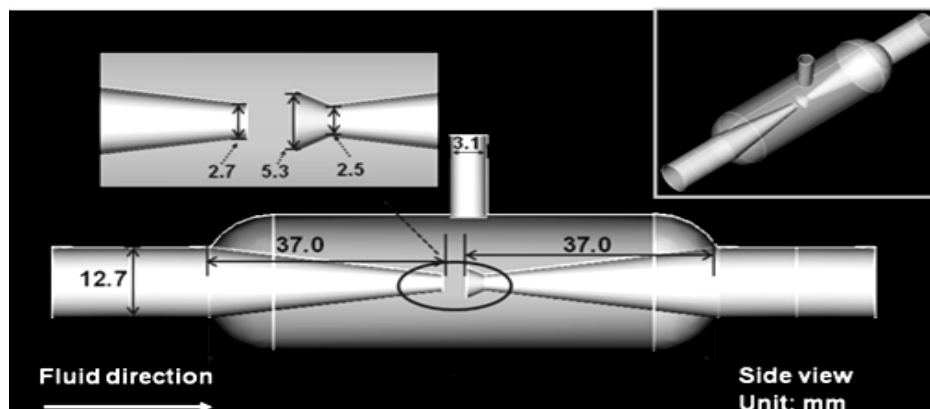


Figure 3-2. Schematic diagram and dimensions of the venturi style cavitation tube.

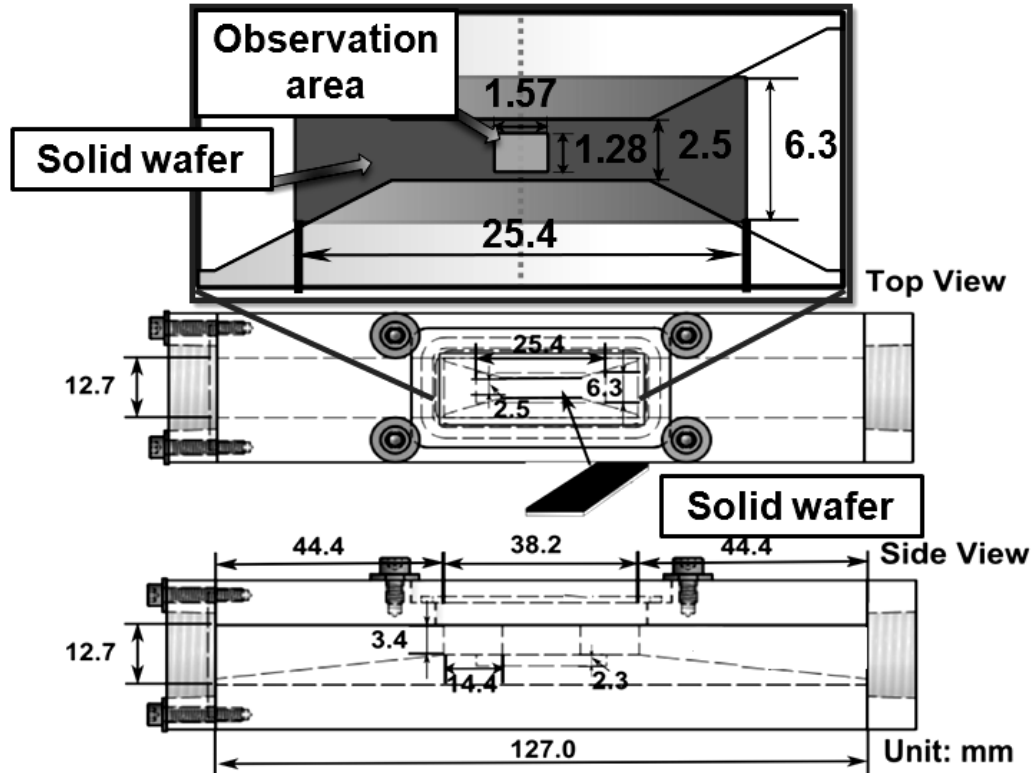


Figure 3-3. Schematic diagram and dimensions of the visualization cell.

The solution is stored in a 1600 ml container. For the investigation of homogeneous nucleation, the size of the bubbles in the container will be measured. The details of the bubble size measurement will be given in the following section. The same container is used to contain the slurry for flotation study of model systems.

3.2 Materials

In this study, de-ionized water (DI water) with resistivity of 10 MΩ was used. And Syncrude process water was used for the bubble aging tests. The composition of the Syncrude process water is listed in Table 1. The alkaline solution, NaOH of 10 mol/L concentration (Fisher Scientific) was used as pH modifier. Silicon wafer from NanoFab at the University of Alberta, galena (Ward's Science) and sphalerite (Ward's Science) were

used for heterogeneous nucleation study. Methyl isobutyl carbinol (MIBC, Sigma-Aldrich) was used as frother, while potassium amyl xanthate (PAX, Sigma-Aldrich) was used as collector to enhance the hydrophobicity of galena and sphalerite. Dichlorodimethylsilane (DDMS $\geq 99.5\%$, Sigma-Aldrich) was chosen to make silicon substrate hydrophobic. Fine grinded silica powder (5 MIN-U-SIL, U. S. Silica) was purchased and used as calibration powder for particle size measurements. Sub-bituminous coal provided by Teck Resources Ltd. was used for solid/bubble interaction tests.

Table 1. Composition of Syncrude process water (ppm).

| Ca ²⁺ | Mg ²⁺ | K ⁺ | Na ⁺ | Cl ⁻ | NO ₃ ⁻ | SO ₄ ²⁻ | HCO ₃ ⁻ | pH |
|------------------|------------------|----------------|-----------------|-----------------|------------------------------|-------------------------------|-------------------------------|-----|
| 33.5 | 16.9 | 23.8 | 508.4 | 389.5 | 3.4 | 87.1 | 741.2 | 8.2 |

3.3 Experimental procedures

Four aspects of the gas nucleation were investigated in this study. First, the micron size bubbles generated by hydrodynamic cavitation in air/water system (homogeneous nucleation) was characterized. Second, a model system for flotation was designed to examine the interaction between micron size bubbles and fine particles. Third, induction timer was used to investigate the effect of the presence of micron size bubbles on the attachment between flotation size bubbles and solid surfaces. Fourth, the gas nucleation on silicon, galena, and sphalerite surfaces (heterogeneous nucleation) was investigated using the flow visualization cell.

3.3.1 Homogeneous nucleation

The cavitation tube was used to generate micron size bubbles in air/water system (homogeneous nucleation). In the experiment, 1400 ml solution was first placed into the 1600 ml container. Then, the remaining air in the circulation system was evacuated by circulating de-ionized water through the loop at throat velocity of 2 m/s. Once all of the air in the circulation system had been evacuated, the throat velocity was raised up to the desired velocity. After the flow loop was running at desired velocity, the bubble size measurement started.

3.3.2 Image analysis method

Image analysis method was used to measure the size of the bubbles generated by hydrodynamic cavitation. During the measurement, the silicon substrates with contact angle of 96° were glued onto the bottom of a Teflon dish and immersed into 1600 ml container for 5 seconds to collect the micron size bubbles. During the collection, the inclination angle of the silicon substrate was fixed at 45° and magnetic stir bar was used to disperse the micron size bubbles, as shown in Figure 3-1. Thereafter, the Teflon dish was turned over, and taken out of the solution with caution. Bubbles attached to the hydrophobic silicon substrates were captured under the optical microscope (Olympus, DP 72). The maximum resolution of the image system is $1.25\ \mu\text{m}$, which means that bubbles with diameters less than $1.25\ \mu\text{m}$ could not be detected. The diameter of the bubbles in the images taken by the optical microscope was calculated by an in-house coded MATLAB script. It should be noticed that, as bubbles attached to the silicon substrate, they deformed,

making the diameters on the images different from the actual bubble diameters. To correct this, a correction approach is applied using the following equation:

$$D_{cor} = 0.767 \times D_{dec} \quad (3.1)$$

where, D_{dec} is the bubble diameter detected; D_{cor} is the bubble diameter after correction. 0.767 is the calculated correction coefficient for $\theta = 96^\circ$. The details of the correction procedures are demonstrated in Appendix A.

3.3.3 FBRM measurement

FBRM, which is an in-situ particle/droplet size measurement technique, was used to determine the size and counts number of micron size bubbles. The FBRM method has been widely used to determine the particle/droplet size in various areas, such as crystallization, suspensions, emulsions, granulation (Kail et al., 2008; Becker et al., 2013; Kumar et al., 2013).

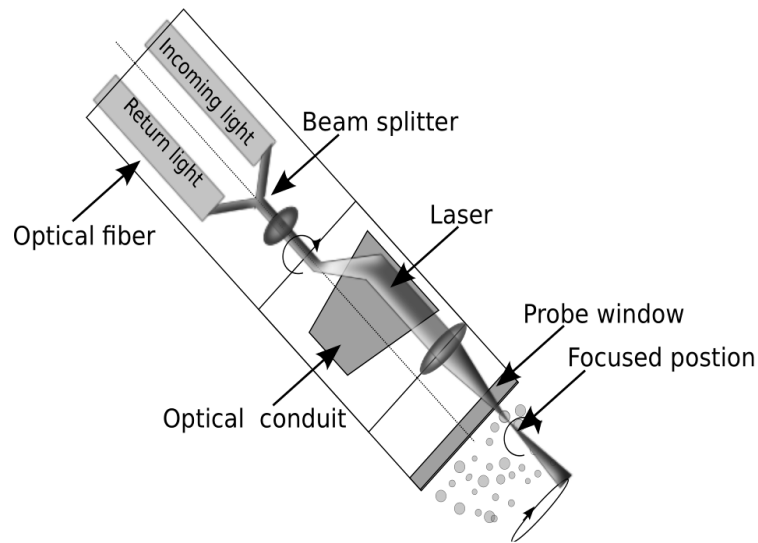


Figure 3-4. Schematic diagram of the FBRM probe.

The FBRM mainly consists of two components: a red laser generator and a detection probe. Schematics of the FBRM optical lens in the optical probe are shown in Figure 3-4. According to the FBRM user manual, to obtain optimum measurement accuracy, the FBRM probe was placed at an angle of 75° , relative to horizontal axis. The corresponding detection window for FBRM ranges from $0.5 \mu\text{m}$ to $1000 \mu\text{m}$. The FBRM detects the chord length rather than the diameter of bubbles. It is known that for a given particle, the average of its chord lengths is less than its diameter. However, from the statistical point of view, such a difference is small and negligible for spherical particles (Kail et al., 2009). In the following, the number based (D_{10}) and Sauter (D_{32}) mean diameters from image analysis are reported. For comparison, the number based (D_{c10}) and Sauter (D_{c32}) mean chord lengths obtained from FBRM are reported.

Comparison between image analysis method and FBRM

The comparison between image analysis and FBRM methods was accomplished in de-ionized water at the throat velocity from 5.7 m/s to 12.7 m/s . The corresponding bubble size distributions, the number based (D_{10}) and Sauter (D_{32}) mean diameters of the number based and Sauter mean chord length, which are denoted as D_{c10} and D_{c32} , are shown in Figure 3-5 and Figure 3-6, respectively. The bars in Figure 3-6 represent the particle size range. The top part of the bar stands for D_{80} , while the bottom part of the bar stands for D_{20} . It can be seen from Figure 3-6 that the bubble size obtained from the FBRM method has a good agreement with those obtained using the image analysis method. However, a small group of short chord lengths ($<5 \mu\text{m}$) detected by FBRM were not detected in the image analysis method. So far, it is still difficult to determine whether these short chord lengths

come from the edge of bubbles with diameter larger than 5 μm or actually from bubbles with diameter less than 5 μm (Kail et al., 2008; Kail et al., 2009).

Figure 3-7 shows that the FBRM method can also qualitatively determine the bubble number density, which cannot be obtained using image analysis method. As anticipated, the number of bubbles increased from 260 to 7570 with increasing throat velocity from 8.0 m/s to 12.7 m/s, indicating the enhancement of hydrodynamic cavitation with increasing fluid velocity. It can be seen that, in addition to the size of the micron size bubbles, FBRM method is able to qualitatively determine the number counts of micron size bubbles, which image analysis method cannot afford. Therefore, FBRM is adapted in the following studies.

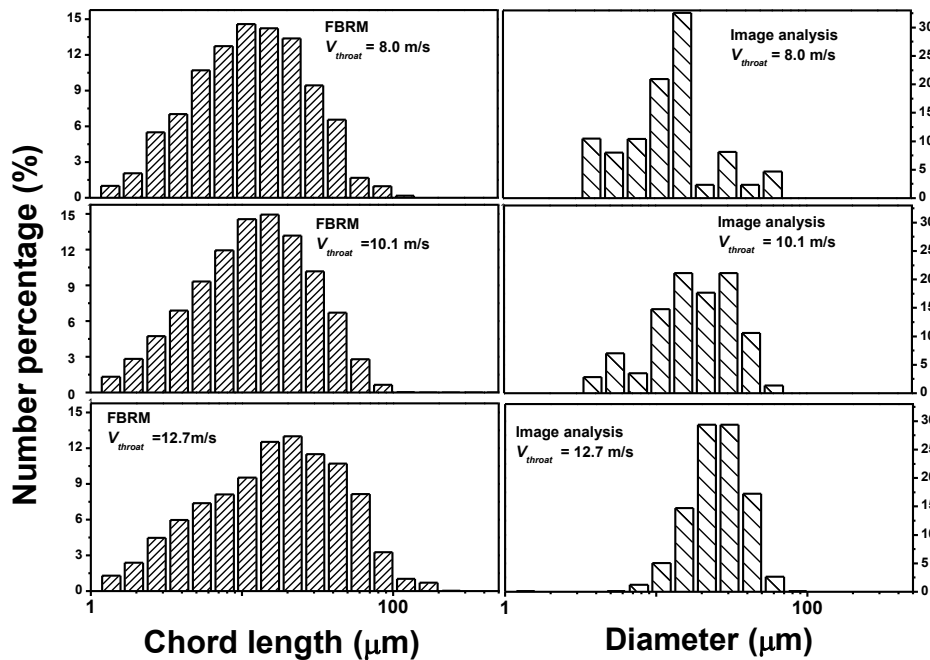


Figure 3-5. Comparison between bubble size distributions obtained using the FBRM and image analysis methods.

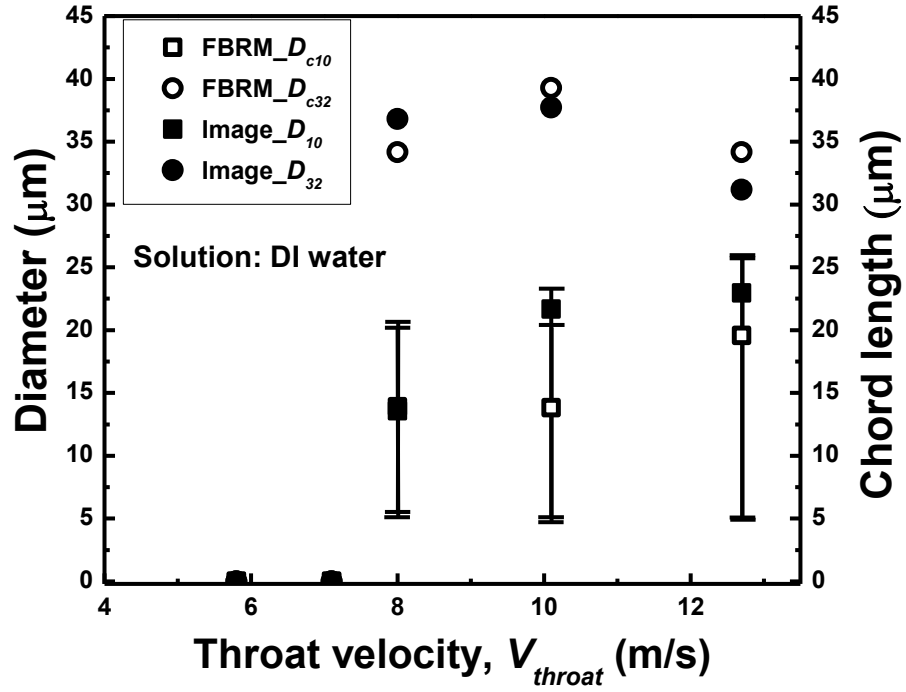


Figure 3-6. Bubble size and chord length as a function of throat velocity.

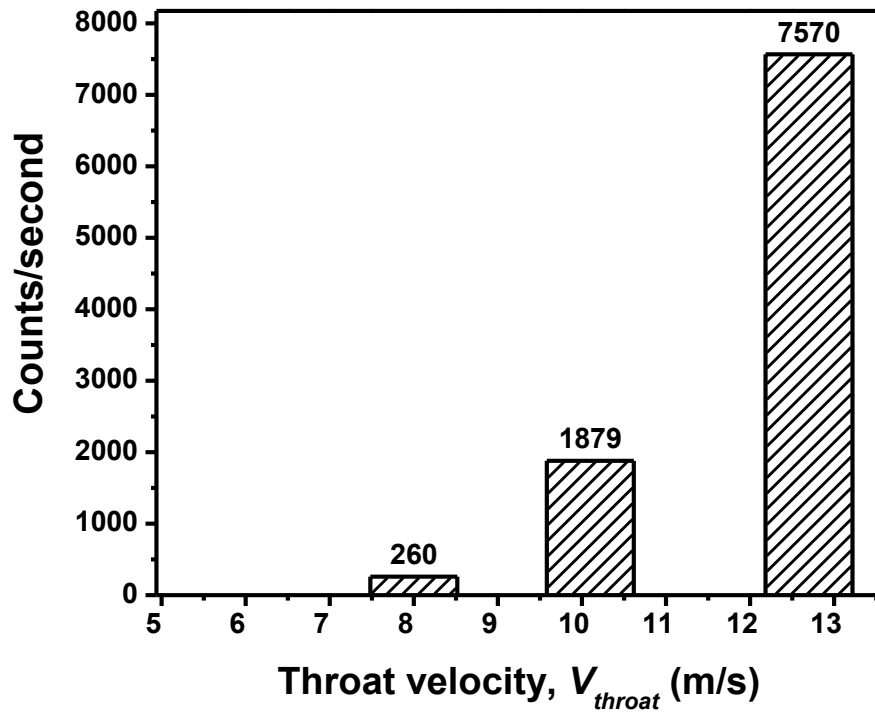


Figure 3-7. Bubble number counts by FBRM in DI water as a function of throat velocity.

3.3.4 Model system used for flotation study

A model system was designed to study the interaction between fine particles and micron size bubbles in flotation. The procedures of the model system are similar to those of conventional flotation. To test the role of hydrodynamic cavitation in the fine particle flotation, only micron size bubbles generated by hydrodynamic cavitation were employed. Although, the term, recovery, was used in the report of the model system to float fine particles in the system, the meaning of the recovery in the model system is different from that in the conventional flotation, as it is mainly to illustrate the prediction of micron size bubbles on fine particles by hydrodynamic cavitation. In fact, the recovery of model system was used as an indicator to evaluate the interaction between micron size bubbles and fine particles (i.e fine coal). The knowledge obtained from model system is intended to be used as guidelines for the design of advanced bubble generator rather than practical flotation.

Fine coal preparation

Chunks of hydrophobic sub-bituminous coal provided by Teck Resources Ltd. were used for particle/bubble interaction test. All of coal chunks were first hammer-crushed to coarse size particles of sizes less than 1 mm. Coarse particles were then further dry ground into fine particles by a laboratory ball mill (Retsch, PM 100 CM) operating at 400 rpm for 30 minutes. To ensure that the fine coal was representative, the coal was well homogenized before and after grinding. To prevent the oxidation of the coal sample, the fine coal was carefully sealed in sample bags and stored in freezer at -18 °C. The particle size distribution of the fine coal was measured using the Mastersizer 3000 (Malvern,

Worcestershire UK). The particle size distribution of the fines is shown in Figure 3-8. The D_{50} of the fine coal was found to be $11.1 \pm 2.8 \mu\text{m}$.

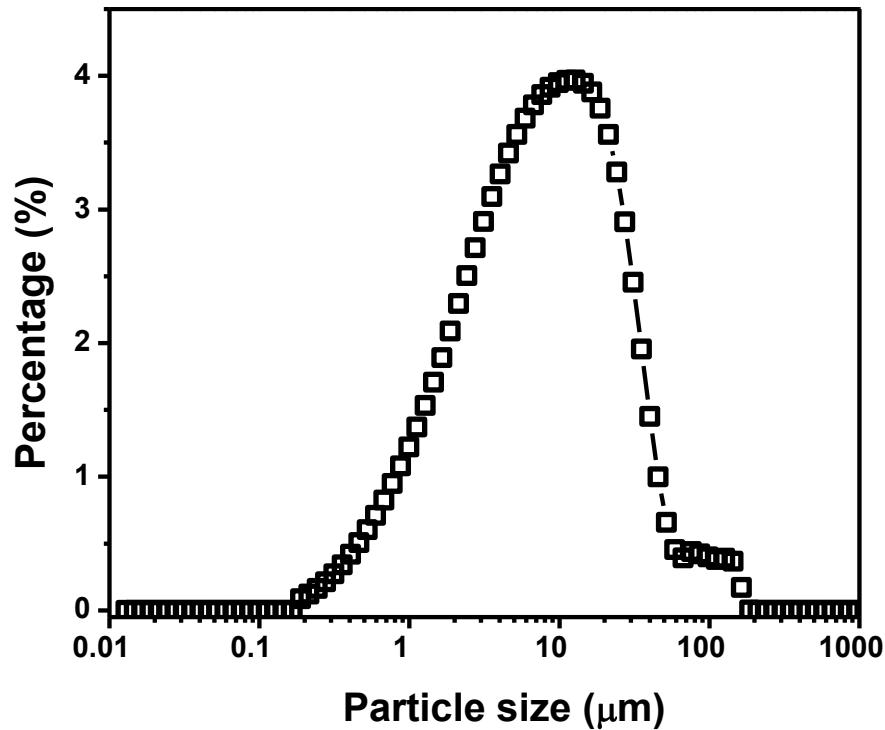


Figure 3-8. The particle size distribution of fine coal.

Procedures of model system flotation

The setup of the model flotation system is similar to that of bubble size measurement, as shown in Figure 3-1. The only difference is that the de-ionized water was replaced with the coal slurry. The volume of the slurry remained at 1400 ml. To fully disperse the fine coal, the slurry was agitated by magnetic stirring bar for 8 hours to obtain well-distributed slurry in a beaker. To evacuate the residual air in the system, the slurry was first pumped into the cavitation tube at throat velocity of 2 m/s. After the air was removed, the fluid velocity at the throat was increased to the desired speed. Then, the fine particles floated to the top of

the slurry were collected at the rate of 16 times per minute. Collected particles were filtered, dried and weighed. The reproducibility of data was also examined at the throat velocity of 10.1 m/s.

Coal oxidation

To study the effect of hydrophobicity of fine particles on the particle/bubble interaction, the hydrophobicity of the fine coal was reduced by oxidation. During oxidation, the fine coal spread on glass dishes (Diameter: 10 cm) were heated to 170 °C in an oven. To maintain the oxygen level in the oven, a vacuum pump was used to circulate air in the oven at 5 ml/min flow rate. Fine coal with different oxidation levels could be obtained by varying the oxidation time. To characterize the hydrophobicity of the fine coal before and after oxidation, the contact angles of polished coal chunks and compressed coal pellets were measured. The experimental results are shown in Figure 3-9. It can be seen that the hydrophobicity for both of the compressed coal pellets and the polished coal chunks reduced when oxidation time was extended, which agrees well with the results of previous studies (Xu and Yoon, 1989; Pawlik et al., 2004). Figure 3-9 also shows that the contact angle of the polished coal chunks was less than that of the compressed coal pellets. According to Laskowski (2001), the air, which is trapped in the pores of the compressed coal pellets, would exaggerate the contact angle of the compressed coal pellets. On the other hand, the surface roughness of the compressed coal pellets may also lead to an overestimation of the contact angle of the compressed coal pellets. The contact angle on polished coal chunks would be more representative of true contact angle.

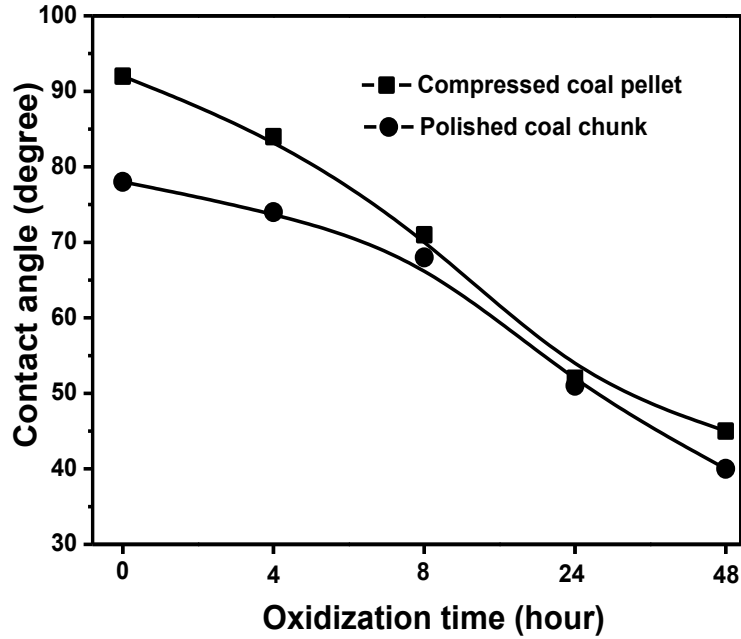


Figure 3-9. Contact angle of compressed coal pellet and polished coal chunk.

3.3.5 Induction timer

The induction timer is widely used to characterize the bubble/solid attachment. The bubble/solid attachment process between a bubble and a solid surface consists of three steps: (a) thinning of liquid intervening film between bubble and solid surface; (b) a sudden rupture of the intervening liquid film and establishment of three-phase contact line; (c) expansion of the three-phase contact line. In current study, the induction time measured is the summation of the three time intervals:

$$t_{ind} = t_t + t_r + t_e \quad (3.2)$$

where t_{ind} stands for the induction time; t_t , t_r and t_e are the time for the corresponding three steps, (a) - (c).

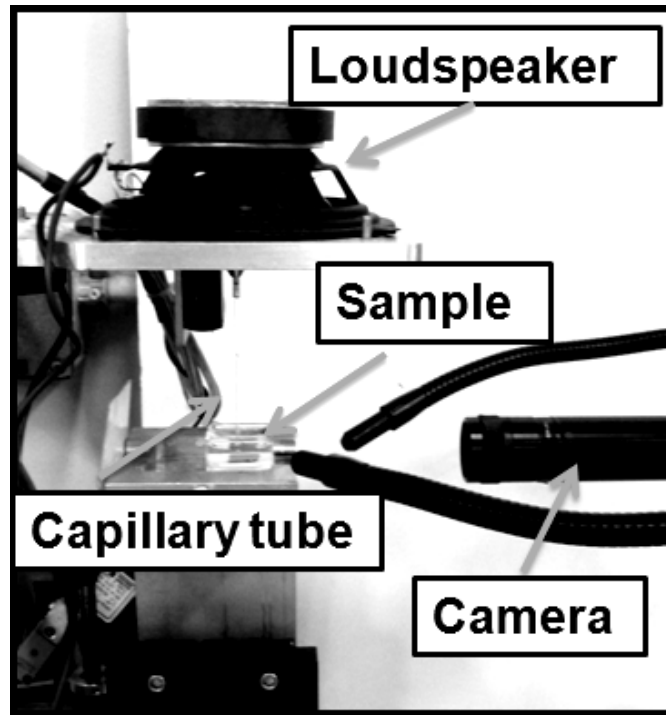


Figure 3-10. Photograph of induction timer used in this study.

In this study, the induction time was measured using an in-house built induction timer. A photographic view of the induction timer setup is shown in Figure 3-10. The components of the induction timer include: a loudspeaker, a mechanical 3D translation stage for positioning, capillary tube, a camera, and light sources. During the measurement, a bubble with diameter of 1.5 mm was generated on the tip of a glass capillary tube and its displacement was controlled using a loudspeaker. By programming the driving voltage of the loudspeaker, the approach velocity, the extent of displacement, contact time, and retraction velocity of the bubble could be accurately controlled. According to previous study (Gu et al., 2003), the approach and retraction velocities of 40 mm/s were used, while the contact time was varied. The attachment probability at given contact time was obtained based on 20 contacts. The induction time is defined as the attachment time when the

attachment probability is equal to 50 %. More details regarding the operating instruction can be found in the reference, Gu et al. (2003).

3.3.6 Degassing and CO₂ saturation

Wei et al. (2009) demonstrated that the dissolved gas content is crucial to the gas nucleation. To remove the dissolved gas in de-ionized (DI) water, the de-ionized water was heated to 80 °C for 2 hours, and then cooled down to room temperature (Zhou et al., 2010). To prevent the air re-entrainment during cooling, the de-gassed water was cooled down in well-sealed bottles. This method cannot totally remove the dissolved gas, and a small amount of dissolved air is still expected to remain in the solution. To increase the dissolved gas content, a soda maker (Soda stream) was used to saturate CO₂ into the solution. The soda maker saturates the CO₂ into the DI water by injecting CO₂ gas stream into the DI water in a sealed plastic bottle. The saturation pressure is controlled using a check valve, which means the saturation pressure of the soda maker is unchangeable. The dissolved CO₂ content was reduced to a pre-set level through dilution. The actual CO₂ content in the solution was measured using a Total Carbon Analyzer (Shimadzu Corporation, 604-8511). Figure 3-11 shows the dissolved CO₂ contents at various dilution ratios. The dilution ratio is defined as the volume of the CO₂ saturated water to the volume of the CO₂ saturated water and dilution de-ionized water. The square meshed columns in Figure 3-11 represent the dissolved CO₂ content calculated based on the original CO₂ content tested. It can be seen that soda water is able to increase the dissolved CO₂ content up to 748 mg/L. Any desired dissolved CO₂ contents less than 748 mg/L could be obtained through dilution.

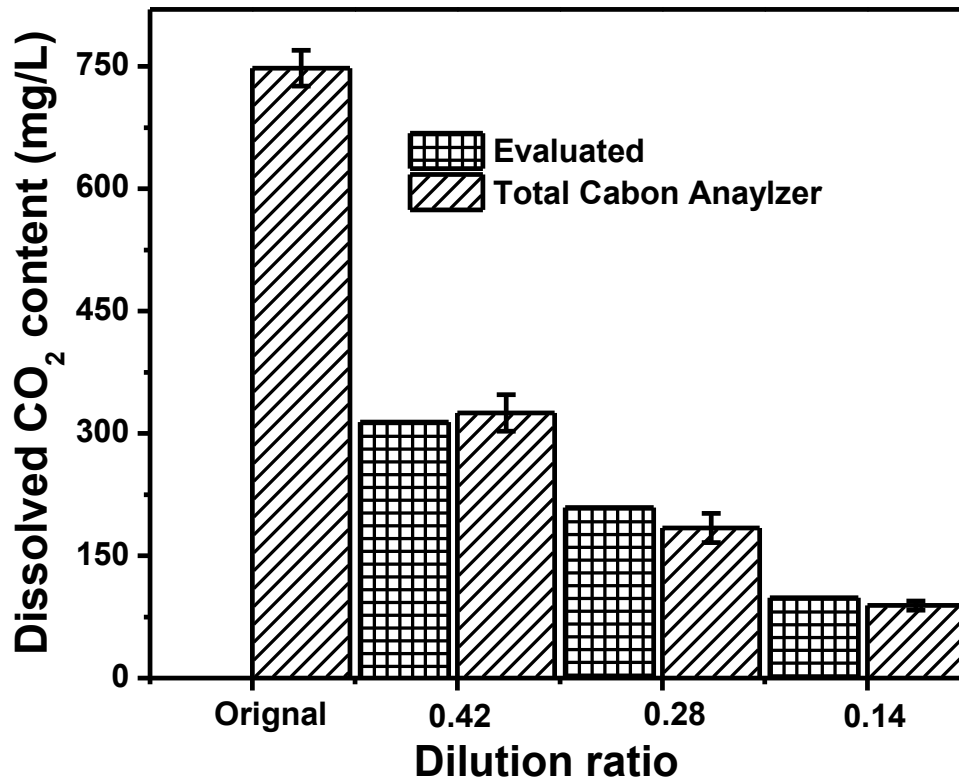


Figure 3-11. Dissolved CO₂ content at different dilution ratios.

3.3.7 Observation of heterogeneous nucleation

The heterogeneous nucleation on silicon wafers, galena and sphalerite surfaces was investigated. The solid wafers were cut to 6.3 mm by 25.3 mm, and then mounted on the bottom wall in the middle of the visualization cell. Then, the solution was slowly pumped into the visualization cell to evacuate the air in the system. After the air was fully evacuated, the fluid velocity was accelerated to the desired level. Thereafter, the optical microscope (Olympus, DP 72) was used to image the solid surface from the top of the flow visualization cell.

3.3.8 Preparation of silicon wafers, galena and sphalerite surfaces

The silicon wafers with contact angle ranging from less than 10° to 96° were used in this study. The silicon wafers were cleaned by immersing them into NaOH solution (pH = 12) for 10 minutes. The contact angle of the silicon wafer cleaned is around 10° , as shown in Figure 3-12 (a), indicating the silicon wafer after cleaning is hydrophilic. Grafting of dichlorodimethylsilane (DDMS) on silicon wafer can increase the hydrophobicity of the silicon wafer. The grafting of the silicon wafer was accomplished by immersing it in 1 mM DDMS toluene solution, and then rinsed with pure toluene. It was found that as the immersing time increased from 10 s to 60 s, the contact angle of the silicon wafer increased from 37° to 96° , correspondingly.

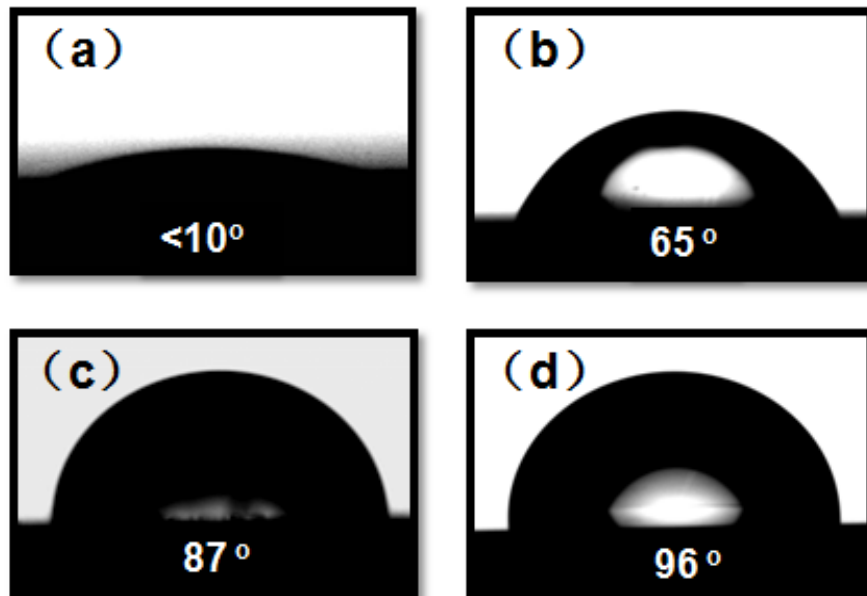


Figure 3-12. Contact angle of the silicon wafer before and after DDMS coating.

Galena and sphalerite surfaces were also used for heterogeneous nucleation tests. To make the galena and sphalerite surfaces, the chunks of galena and sphalerite ores were first

gelled in epoxy resin. After hardening, they were then cut into a square that fits the flow visualization chamber. To smooth the galena and sphalerite surfaces, the galena and sphalerite surfaces were polished by 1200/1600 grits sand paper. To increase the hydrophobicity of galena surfaces, the galena surfaces were immersed in potassium amyl xanthate (PAX) solution of 10^{-6} M to 10^{-3} M concentration at pH = 6.5 for 5 minutes. It was found that with increasing the concentration of PAX, the contact angle of galena surfaces increased from 44 ° to 83 °; Sphalerite surfaces were first activated by 10^{-4} M CuSO_4 for 5 minutes, and then immersed in PAX solution of 10^{-6} M to 10^{-3} M concentration at pH = 6.5 for 5 minutes. In this way, the contact angle of sphalerite surfaces increased from 24 ° to 87 °. It should be stressed that the contact angles reported are based on the measurement using DSA.

Chapter 4

Results and Discussion

4.1 Effect of fluid velocity on homogeneous nucleation

In this section, the size and number counts of bubbles generated by hydrodynamic cavitation in de-ionized (DI) water (homogeneous nucleation) at various throat velocities were determined. The size distributions of the bubbles in DI water at throat velocity from 8.0 m/s to 12.7 m/s are reported in Figure 4-1. The corresponding number mean (D_{10}) and Sauter mean (D_{32}) diameters, and the number and Sauter mean of chord lengths, which are denoted as D_{c10} and D_{c32} , are shown in Figure 4-2. The variation of the number counts of bubbles as a function of throat velocity is shown in Figure 4-3.

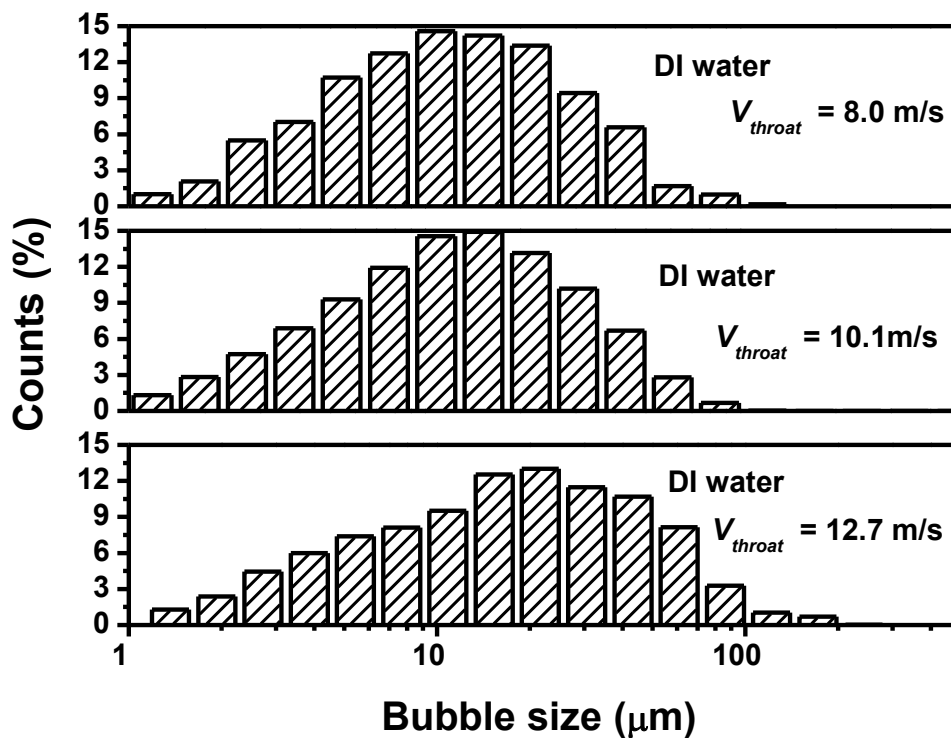


Figure 4-1. Bubble diameter distribution as a function of throat velocity.

Figure 4-1 shows that for the entire throat velocity range tested, the bubble size distributions are always monomodal. From Figure 4-2, it can be seen that no bubbles were detected until the throat velocity reached 8.0 m/s. Thus, the on-set throat velocity in this case was determined to be 8.0 m/s. Zhou (1996) reported that the on-set velocity for a cavitation tube with diameter of 2.35 mm in tap water was 8 m/s, which is in a good agreement with the on-set velocity obtained here. It should be kept in mind that the on-set velocity for a venturi style cavitation tube tends to increase with reducing the cross section area of the cavitation tube due to higher energy loss in a cavitation tube with smaller cross section area at the throat (Zhou, 1996; Zhou et al., 2009). Thus, only the on-set velocities of cavitation tubes with similar cross section areas are comparable. Figure 4-2 also shows that number mean of chord length, D_{c10} increased slightly from 13.9 μm to 19.5 μm as the throat velocity increased from 8.0 m/s to 12.7 m/s (the top and bottom of the range bars in Figure 4-2 represent the D_{80} and D_{20} of the size distribution, respectively). And, the corresponding Sauter mean of chord length, D_{c32} increased from 34 μm to 39 μm . It can be seen that the variation of throat velocity has little effect on the bubble size. This observation is consistent with that from Finch et al. (2008). And, Rodrigues and Rubio (2003, 2007) summarized that Sauter mean of the bubbles generated by hydrodynamic cavitation normally ranged from 10 μm and 100 μm at room temperature. As demonstrated, the Sauter mean of chord length, D_{c32} is equivalent to Sauter mean, so the sizes of bubbles observed here are consistent with the results from previous studies. Figure 4-3 shows that the increase in fluid velocity led to an increase in the number counts of micron size bubbles. Similar results were also observed by Zhou (1996).

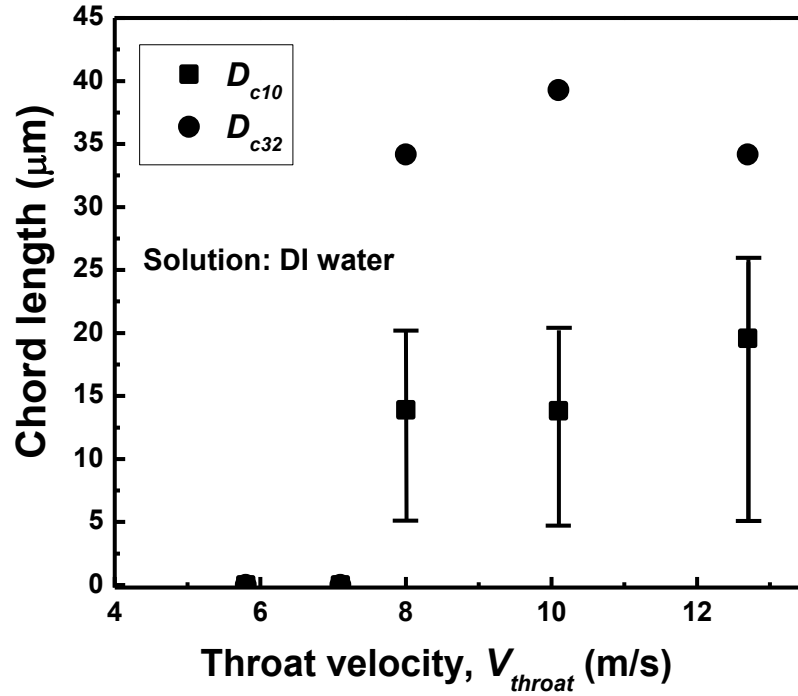


Figure 4-2. Number mean of chord length, D_{c10} and Sauter mean of chord length, D_{c32} as a function of throat velocity.

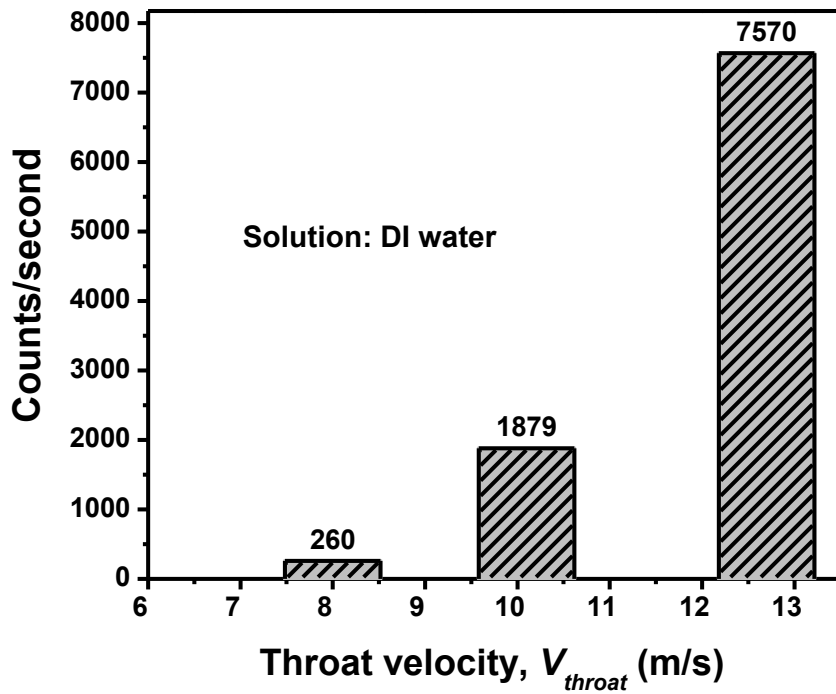


Figure 4-3. Number counts of bubbles as a function of throat velocity.

4.2 Effect of dissolved gas content on homogeneous nucleation

The size and number counts of bubbles generated by hydrodynamic cavitation in degassed water were determined. The size of bubbles in degassed water with the increase in throat velocity is reported in Figure 4-4. The definitions of the symbols in Figure 4-4 are identical to those in Figure 4-2. While, the corresponding number counts of bubbles generated in degassed water are shown in Figure 4-5.

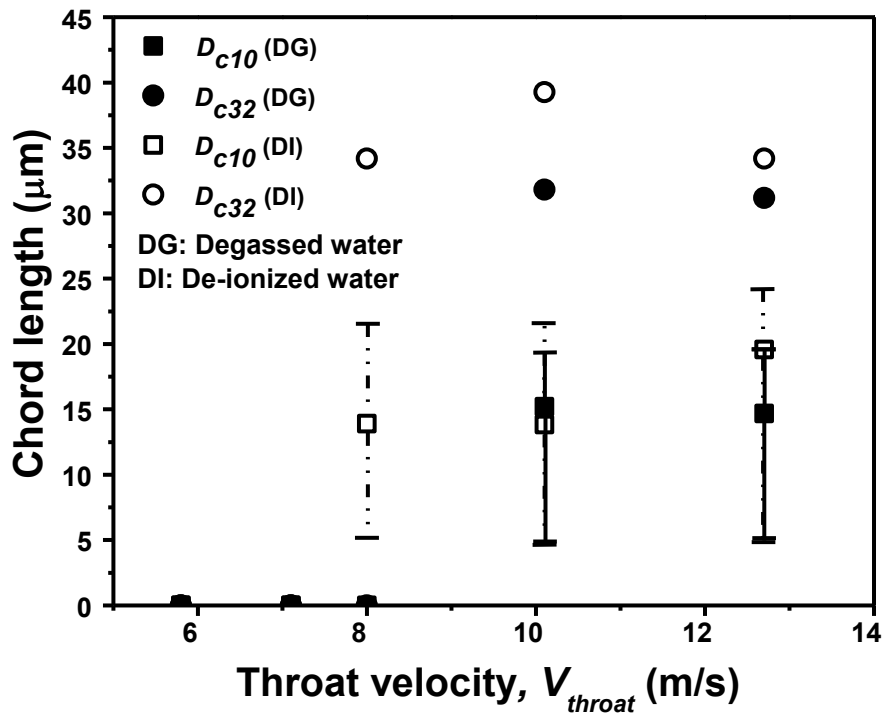


Figure 4-4. The number mean of chord length, D_{c10} and Sauter mean of chord length, D_{c32} as a function of throat velocity in degassed water.

By comparing the results in Figure 4-2 and Figure 4-4, we can find that degassing the de-ionized (DI) water increased the on-set velocity of hydrodynamic cavitation from 8.0 m/s to 10.1 m/s. Reviewing equations of (2.1) and (2.2), we can find that degassing led to the decrease in super-saturation ratio, S , indicating a higher minimum Gibbs energy for gas

nucleation, ΔG^* in degassed water. The on-set velocity is expected to increase with the increase in minimum Gibbs energy for gas nucleation. Lee and Choi (2003), Wei et al. (2009) and Zhou et al. (2009) also observed increase in on-set velocity for hydrodynamic cavitation with decreasing dissolved gas content by degassing. Figure 4-4 shows the number mean of chord lengths, D_{c10} between throat velocities of 10.1 m/s to 12.7 m/s in degassed water was around 15 μm , which are similar to their counterparts in DI water. In contrast, the sauter means of chord length, D_{c32} remained constant at 31 μm , which are slightly smaller than that in DI water. Figure 4-5 clearly shows that degassing of DI water significantly reduced the number counts of bubbles generated compared to that in DI water.

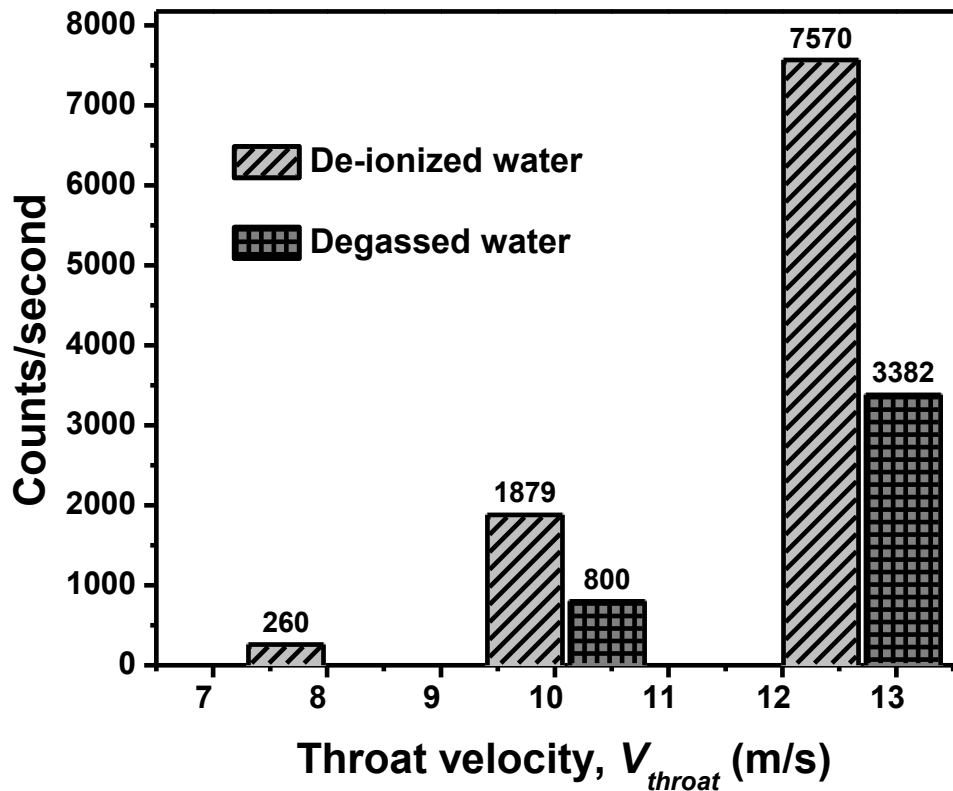


Figure 4-5. Number counts of bubbles generated in degassed water as a function of throat velocity.

In the following, the effect of CO₂ saturation on the size and number counts of bubbles was examined. In this experiment, the concentration of the dissolved CO₂ content was increased from 89 to 320 mg/L, while the throat velocity kept at 10.1 m/s. Figure 4-6 shows the variation of bubble size with increasing dissolved CO₂ content. The variation of the number counts of bubbles is reported in Figure 4-7. As shown in Figure 4-6, D_{c10} remained almost constant around 10 μm with increasing dissolved CO₂ content, while D_{c32} increased slightly from 32 μm to 36 μm as the dissolved CO₂ content was increased. Therefore, similar to the case in degassed water, increasing the dissolved CO₂ content does not lead to an obvious change in bubble size. However, as shown in Figure 4-7, the increase in the dissolved CO₂ content led to an increase in the number counts of bubbles. Lee and Choi (2003), Wei et al. (2009) and Zhou et al. (2009) showed that increasing dissolved gas content increased the bubble generation rate.

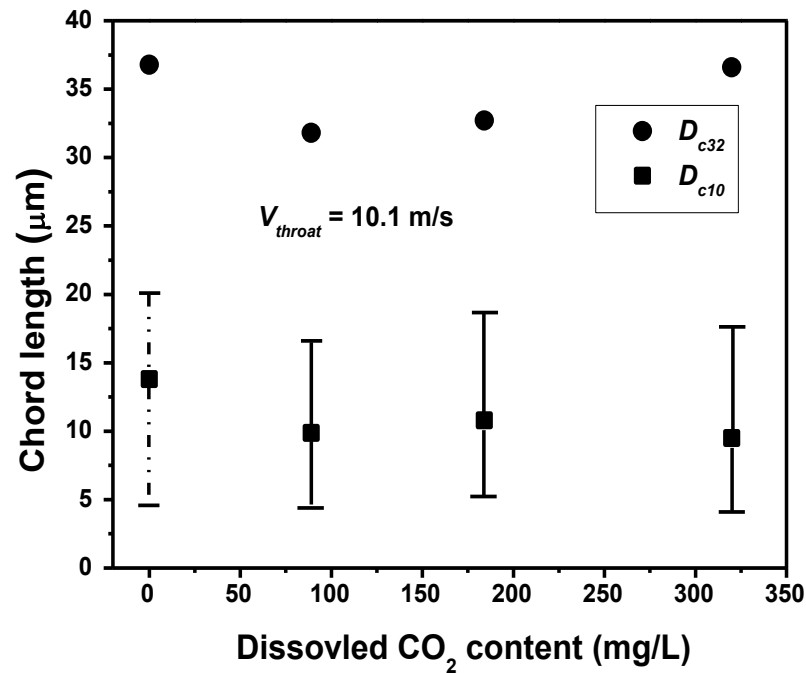


Figure 4-6. Number mean of chord length, D_{c10} and Sauter mean of chord length, D_{c32} as a function of dissolved CO₂ content at throat velocity of 10.1 m/s.

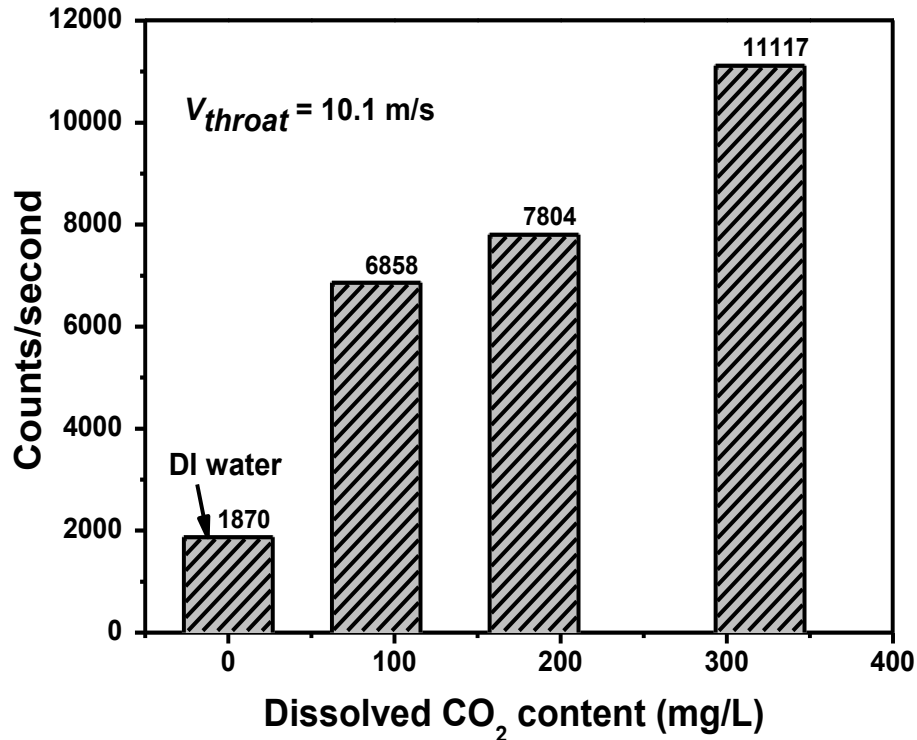


Figure 4-7. Number counts of bubbles as a function of the dissolved CO₂ content at throat velocity of 10.1 m/s.

Thus, it can be seen that varying the dissolved gas content by either degassing or CO₂ saturation does not have significant impact on bubble size. But the number counts of bubbles increase with increasing dissolved gas content.

4.3 Effect of frother addition on homogeneous nucleation

In flotation, small amount of frother (~10 ppm) is added to stabilize bubbles and froth layer. Therefore, it is interesting to investigate the effect of addition of 10 ppm MIBC on the bubble size and number counts of bubbles. The corresponding size and number counts of bubbles with addition of 10 ppm MIBC as a function of throat velocity are shown in Figure 4-8 and Figure 4-9, respectively. Figure 4-8 shows that the on-set velocity of 8.0 m/s for the hydrodynamic cavitation with addition of 10 ppm MIBC is the same as that in de-

ionized (DI) water. According to equations of (2.1) and (2.2), the way that addition of frother affects the minimum Gibbs energy of gas nucleation is by reducing surface tension. However, the decrease in surface tension due to the addition of 10 ppm MIBC is negligible (Wang and Yoon, 2008). Still, no significant change in D_{c10} was found as throat velocity increased from 8.0 m/s to 12.7 m/s. But D_{c32} decreased slightly from 32 μm to 26 μm due to the prevention of bubble coalescence (Wang and Yoon, 2008). Figure 4-9 shows a similar trend that the number counts of bubbles increased with increasing throat velocity. Compared with those in DI water, the number counts of bubbles in 10 ppm MIBC solution were increased. The observed increase in number counts of bubbles with addition of 10 ppm MIBC is attributed to the minimization of the dissolution of micron size bubbles (Wang and Yoon, 2008).

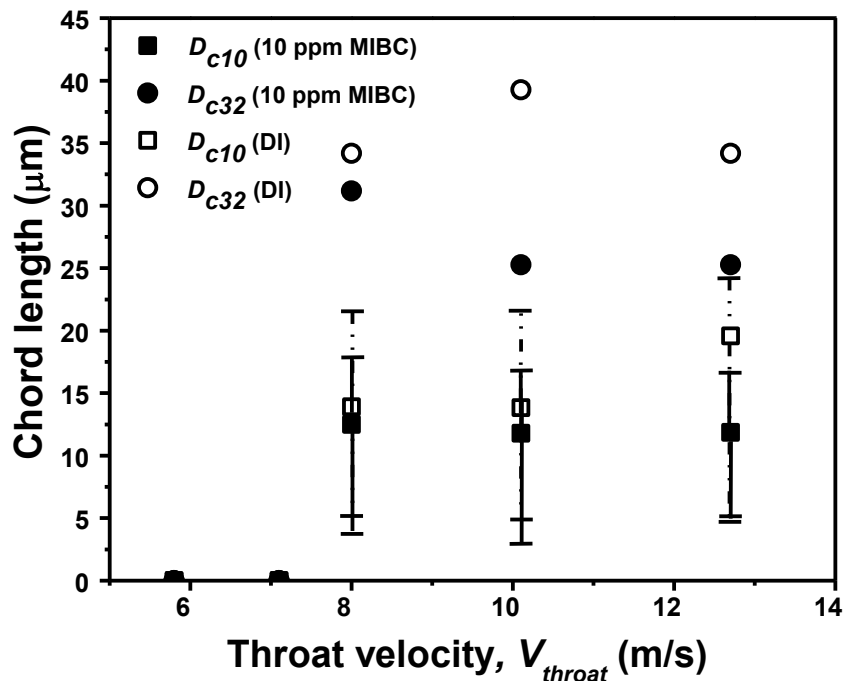


Figure 4-8. Effect of 10 ppm MIBC addition on number mean of chord length, D_{c10} and Sauter mean of chord length, D_{c32} as a function of throat velocity.

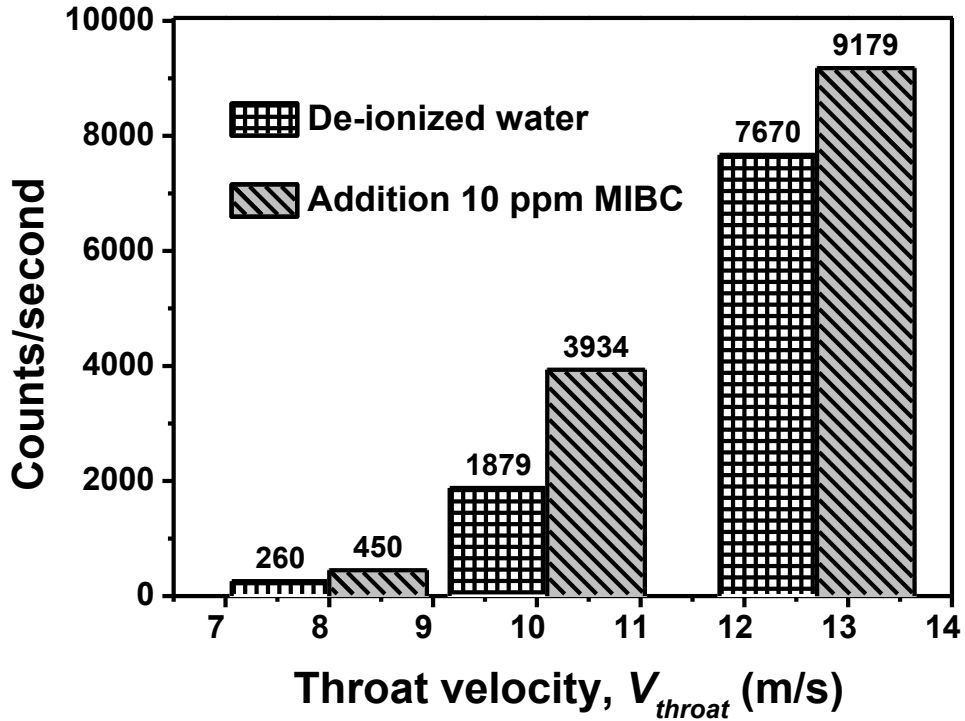


Figure 4-9. Number counts of bubbles as a function of throat velocity with 10 ppm MIBC addition.

4.4 Effect of bubble number density on flotation recovery

In this section, the recovery from 3 % (w/w) coal slurry model system at various throat velocities was determined. Figure 4-10 shows the recovery kinetics of the fine coal as a function of time at various throat velocities. For demonstration purpose, the ultimate recoveries shown in Figure 4-10 are re-plotted in Figure 4-11 as a function of throat velocity. As shown in Figure 4-10, when throat velocity was less than 8.0 m/s, no fine coal was floated. As demonstrated in section 4.1, on-set velocity of 8.0 m/s for hydrodynamic cavitation in DI water. Therefore, the absence of micron size bubbles at throat velocity less than 8.0 m/s accounts for the observation. Another character we can see from Figure 4-11

is that the recovery kinetics started to level off after 6 minutes of flotation. This phenomenon will be further studied in the following.

Figure 4-11 indicates that the ultimate recovery was highly dependent on the throat velocity. In section 4.1, it was shown that the increase in throat velocity led to a growing number of bubbles generated. So, it can be deduced that the increase in the number counts of bubbles caused the recovery enhancement. To identify the froth components, the froth at throat velocity of 10.1 m/s was sampled and examined under optical microscope. One typical image of froth examined is shown in Figure 4-12. From Figure 4-12, we can clearly see that the micron size bubbles generated by hydrodynamic cavitation aggregated the fine coal.

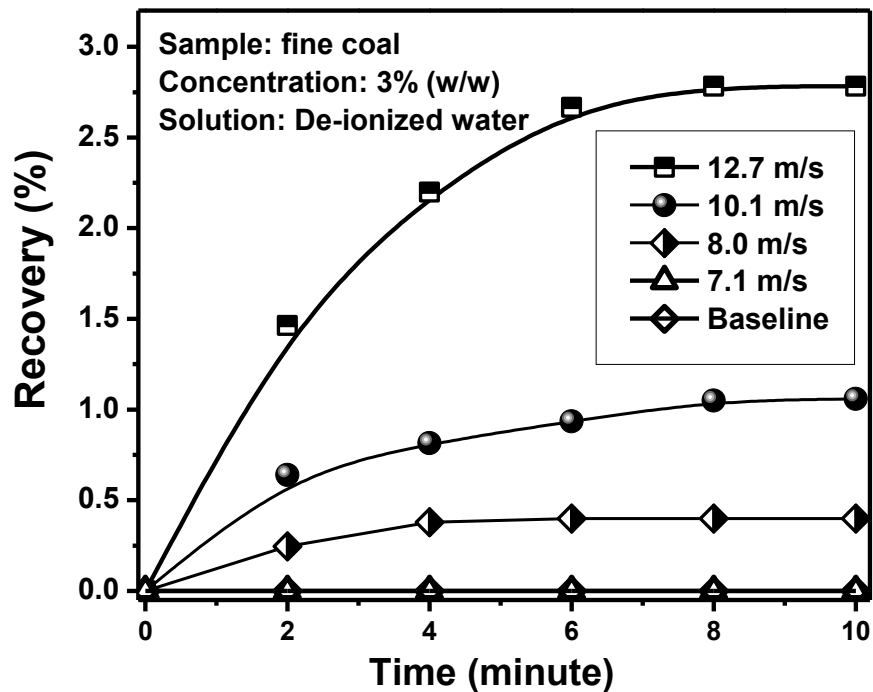


Figure 4-10. Flotation kinetics of fine coal as a function of throat velocity.

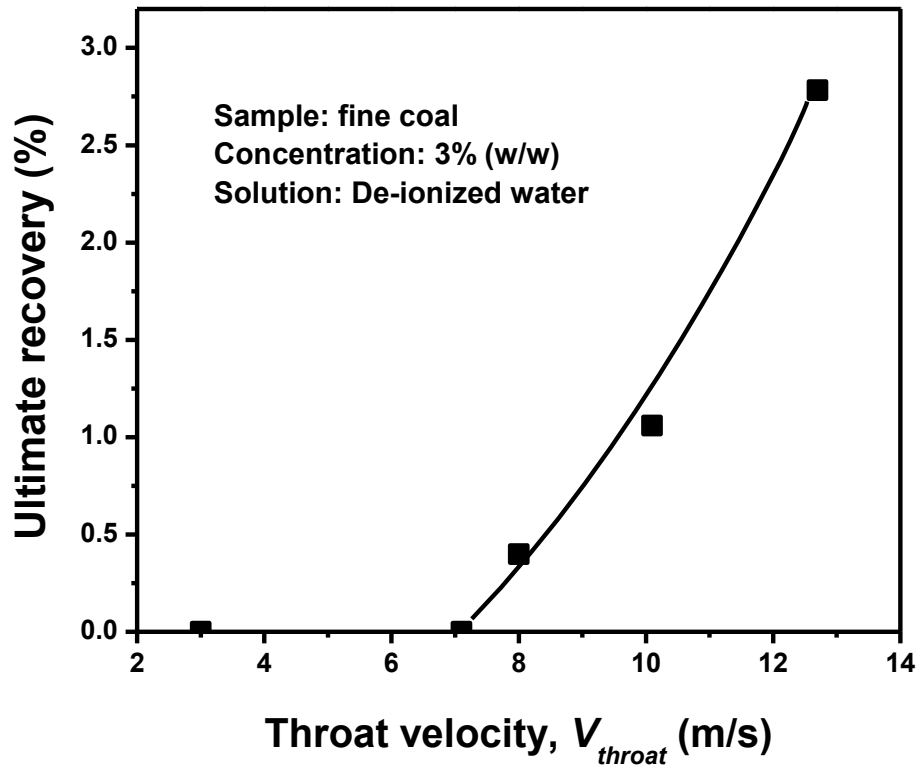


Figure 4-11. Ultimate recovery of fine coal as a function of throat velocity.

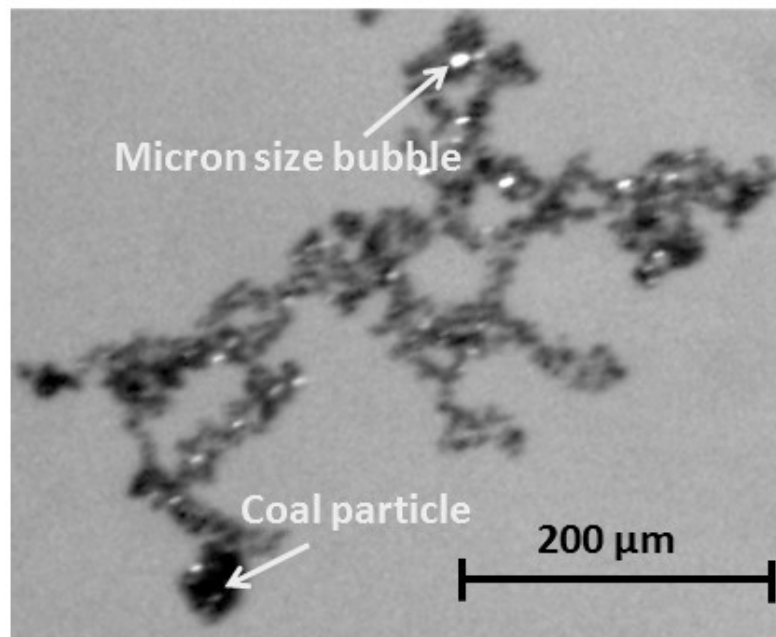


Figure 4-12. A typical image of the froth collected in the model fine coal flotation system.

4.5 Effect of dissolved gas content on flotation recovery

The effect of dissolved CO₂ on fine coal recovery from model system was investigated. The content of the dissolved CO₂ was increased from 89 mg/L to 320 mg/L, while the throat velocity was kept constant at 10.1 m/s. Figure 4-13 shows the flotation kinetics with increasing dissolved CO₂ content, while the corresponding ultimate recovery is presented in Figure 4-14. The results in Figure 4-13 clearly show that the recovery of fine coal increased with increasing dissolved CO₂ content. It is believed that the increase in the number of bubbles, due to the increase in the dissolved CO₂ content, is responsible for the recovery enhancement, as increased number of micron size bubbles increased fine coal aggregation and hence enhanced flotation kinetics.

The recovery for the initial dissolved CO₂ content of 320 mg/L at increased throat velocity was also examined. The flotation kinetics and ultimate recovery are shown in Figure 4-14 and Figure 4-15, respectively. Both figures indicate that, for identical initial CO₂ dissolved gas content, the increase in throat velocity led to the increase in flotation recovery, same as the trend observed in DI water. As shown in Figure 4-14, the recovery kinetics in CO₂ saturated water also leveled off after 6 minutes. To explain this phenomenon, the dissolved CO₂ content after flotation was determined using total carbon analyzer (TCA). It is found that regardless of the initial dissolved CO₂ content, only very small amount of CO₂ is left in the slurry after flotation, which indicates that the depletion of the dissolved CO₂ accounts for the level off of fine coal recovery after 6 minutes of flotation. To investigate the release of CO₂, the variation of the dissolved CO₂ content within 6 minutes was determined. The results are shown in Figure 4-16. The dissolved CO₂ content reduced

gradually as flotation progressed. After 6 minutes of flotation, most of the initial saturated CO₂ was released.

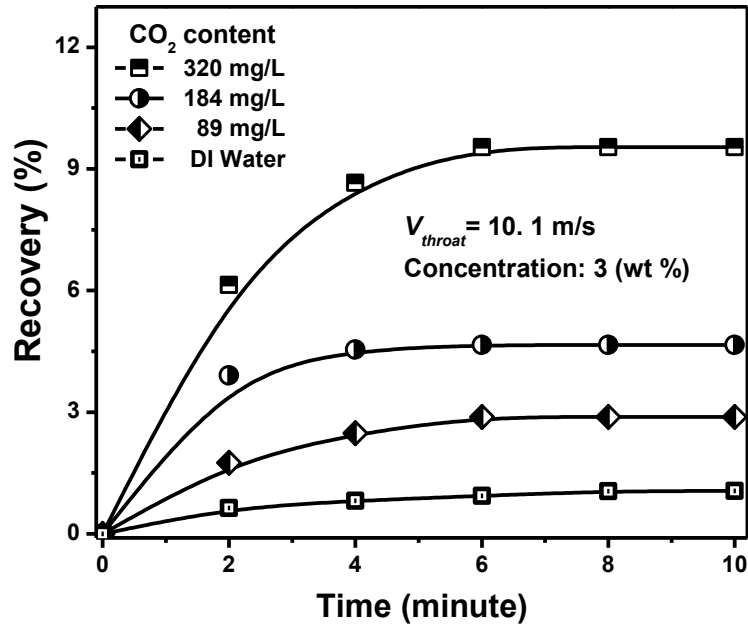


Figure 4-13. Flotation kinetics of fine coal as a function of dissolved CO₂ content.

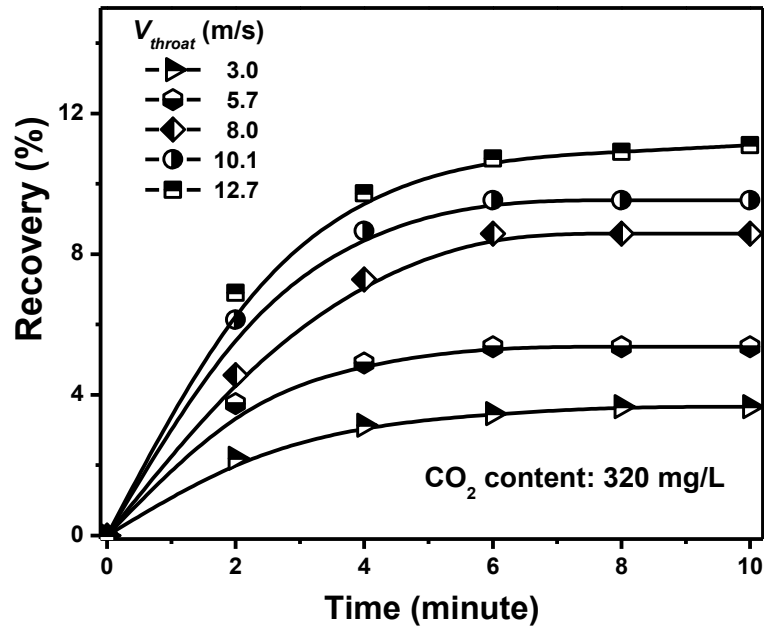


Figure 4-14. Flotation kinetics of fine coal in CO₂ saturated solution as a function of throat velocity.

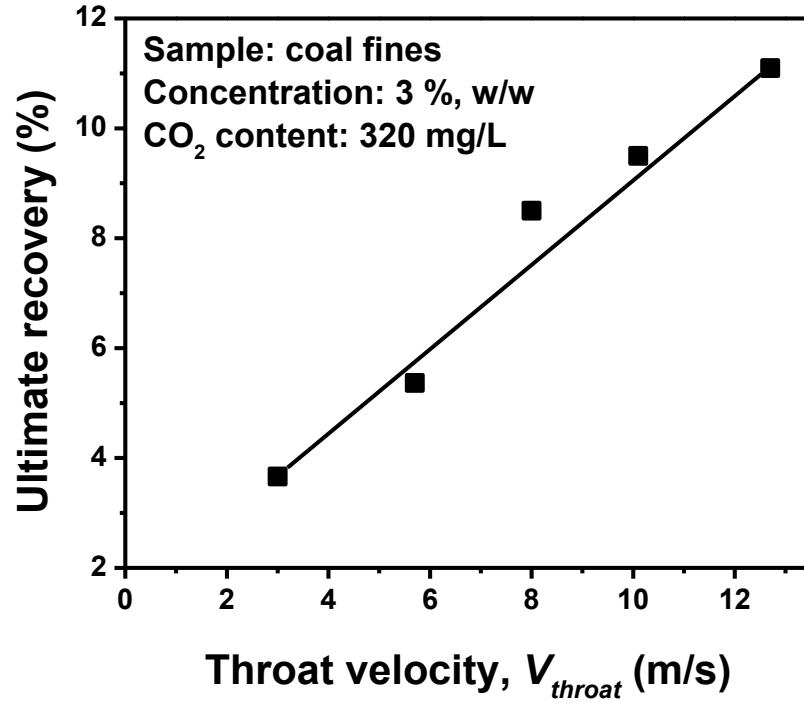


Figure 4-15. Ultimate recovery of fine coal in CO₂ saturated solution as a function of throat velocity.

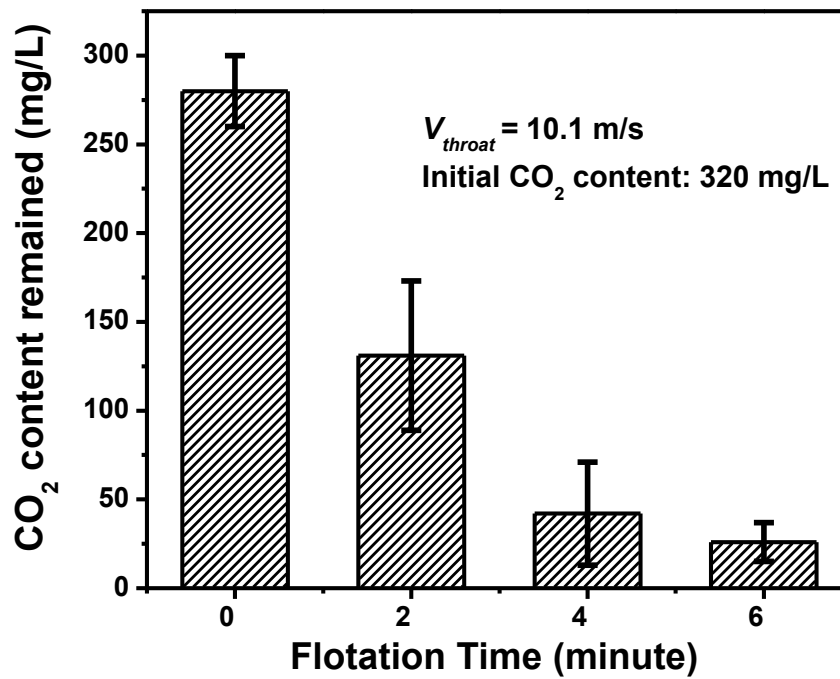


Figure 4-16. Residual CO₂ concentration in the solution as a function of flotation time.

4.6 Effect of external entrained air on flotation recovery

It has been shown that the number counts of bubbles are essential to the flotation recovery. And the number counts of micron size bubbles are associated with the dissolved gas content. Therefore, it is important to investigate whether injecting a small amount of air into the cavitation tube could replenish the dissolved gas content released during model system. If external air entrainment can actually replenish the dissolved gas content, a further increase in the flotation recovery is expected. Flotation kinetics as a function of volumetric air rate is shown in Figure 4-17. In this study, the volumetric flow rate was varied from 1 ml/min to 15 ml/min. Figure 4-17 shows that, at throat velocity of 10.1 m/s, injecting 2.5 ml/min air into cavitation tube increased the recovery from 1.1 % to 11.7 %.

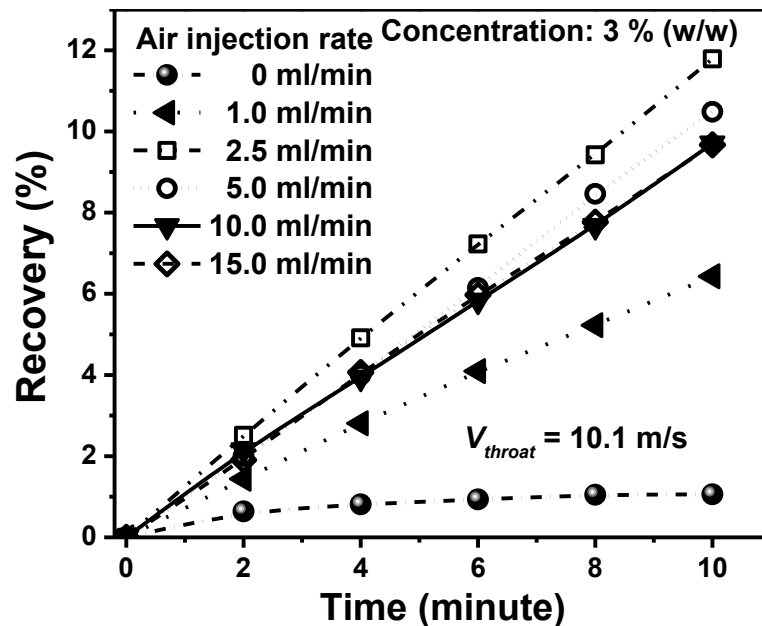


Figure 4-17. Flotation kinetics of fine coal as a function of time for various amount of external air addition into the cavitation tube.

It appears that when air was injected at higher than 2.5 ml/min, air blocks formed inside the cavitation tube, which was detrimental to the flotation. Figure 4-17 also shows that due to the air injection, the flotation recovery increased constantly with flotation time up to 10 minutes tested.

4.7 Effect of hydrophobicity on flotation recovery

Crawford and Ralston (1988), and Koh et al. (2009) showed that the flotation recovery was dependent on surface hydrophobicity. In this section, the fine coal with different oxidation degree was used to illustrate the selectivity of gas nucleation on hydrophobic particles. In this experiment, 320 mg/L CO₂ saturated water was used, and throat velocity was kept constant at 10.1 m/s. The corresponding flotation kinetics is shown in Figure 4-18.

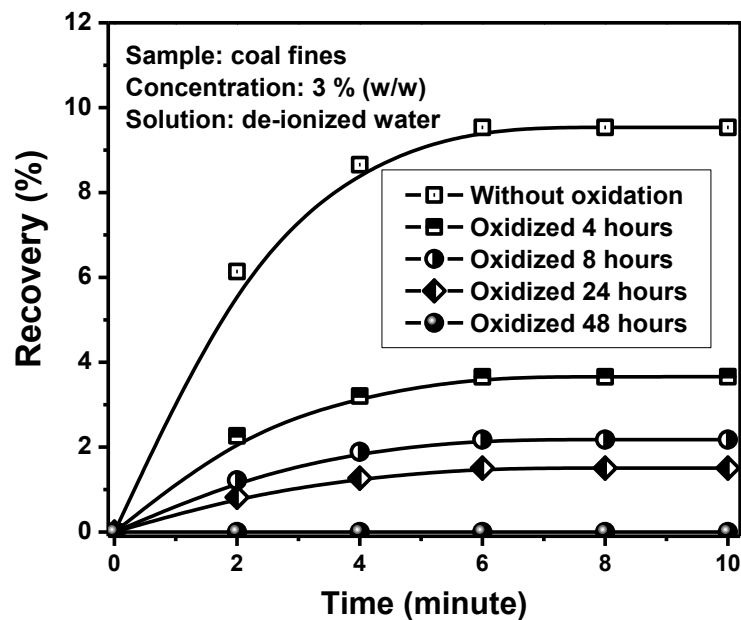


Figure 4-18. Flotation kinetics of fine coal as a function of coal surface hydrophobicity.

To check the experimental results shown in Figure 4-18, the silicon wafers with gradually reduced hydrophobicity were inserted into de-ionized (DI) water in the container and the

throat velocity was kept constant at 10.1 m/s. Typical images of the silicon wafer surface after collection of micron size bubbles generated by hydrodynamic cavitation are shown in Figure 4-19. Figure 4-19 (a) demonstrates that the micron size bubbles could attach to silicon wafer of contact angle of 62° . However, as shown in Figure 4-19 (b), if the contact angle of the silicon wafer was reduced to 45° , no micron size bubbles were collected, which further confirms that the micron size bubbles could not attach to the surface of contact angle equal to or less than 45° . This finding supports the experimental results shown in Figure 4-18.

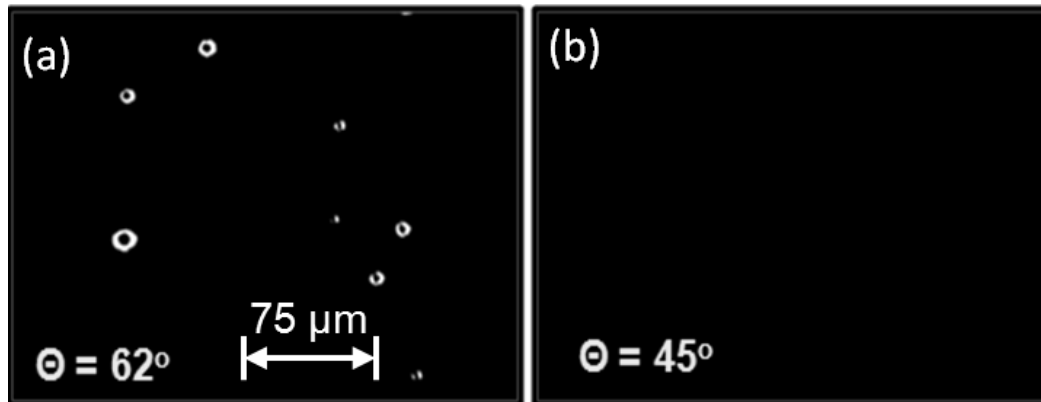


Figure 4-19. Images of silicon wafers with different contact angles after the collection of micron size bubbles. (a) silicon wafer of $\theta = 62^\circ$; (b) silicon wafer of $\theta = 45^\circ$. The throat velocity was kept constant at 10.1 m/s.

4.8 Effect of fine particle concentration on flotation recovery

Figure 4-20 shows the effect of the solid concentration on the recovery of the fine coal model system. It can be seen that the recovery was decreased as the concentration of fine coal increased from 1 % (w/w) to 3 % (w/w). Since the throat velocity remained at 10.1 m/s for the three runs, the number of micron size bubbles generated is expected to be

identical for the three runs. Therefore, the decrease in recovery is attributed to the reduced ratio of the number of micron size bubbles to the number of fine coal with increasing the concentration of fine coal.

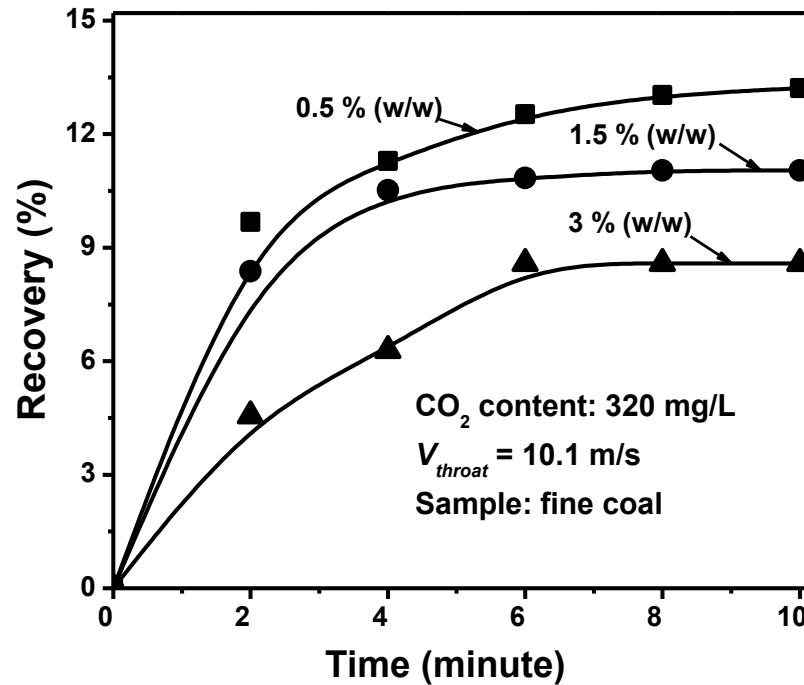


Figure 4-20. Flotation recovery as a function of time for fine coal slurry of three different concentrations.

4.9 Effects of micron size bubbles and bubble aging on bubble/solid attachment

Sobhy and Tao (2013) conducted hydrodynamic cavitation assisted column flotation, and they proposed that the micron size bubbles might function as a secondary collector to enhance the bubble/solid attachment. However, they did not quantify the effect of the presence of micron size bubbles on the attachment between particles and flotation size bubbles. Furthermore, Wang (2013) showed that bubble aging retarded the bubble/solid attachment. In flotation practice, both micron size and flotation size bubbles are possible to be aged. Therefore, it is important to investigate the effect of bubble aging on the bubble/solid attachment. In present study, the effect of the presence of the micron size bubbles on bubble/solid attachment was evaluated by induction time measurement using the systems shown in

Figure 4-21. In this experiment, silicon wafer of contact angle equal to 65° was selected as substrate.

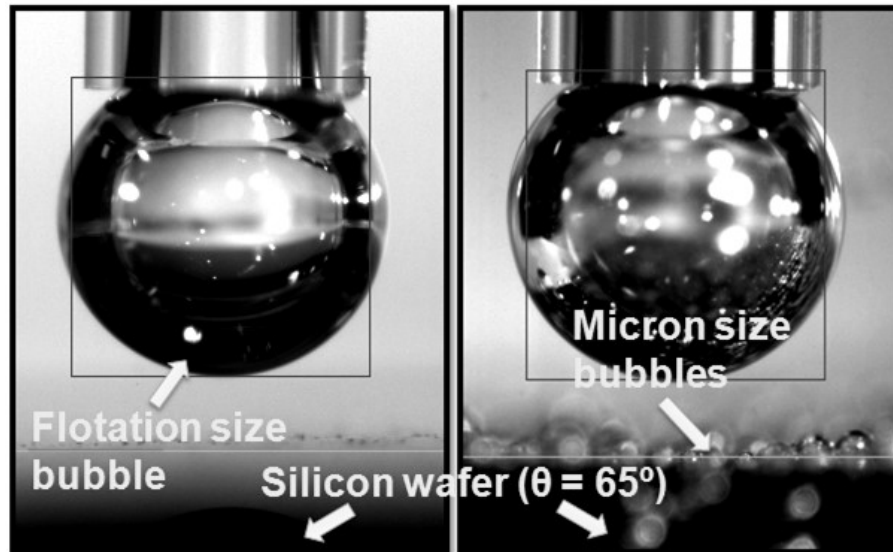


Figure 4-21. Images of induction time experiments with and without micron size bubbles.
(a) Silicon wafer without micron size bubbles; (b) silicon wafer frosted with micron size bubbles.

To investigate the effect of the presence of micron size bubbles on bubble/solid attachment, micron size bubbles were first generated on the silicon wafer. The silicon wafer was glued on the bottom of the cell, and then immersed in the container of the circulation system. The experiment was conducted at throat velocity of 10.1 m/s. In the first part of the investigation, the induction time measurements were conducted immediately after micron size and flotation size bubbles had been generated. Therefore, micron size and flotation size bubbles in this case were considered to be fresh. The corresponding results are shown in Figure 4-22. For both de-ionized (DI) and Syncrude process water systems, the induction time were reduced significantly with the presence of the micron size bubbles on

the solid surface. This indicates that the presence of micron size bubbles greatly enhanced the bubble/solid attachment.

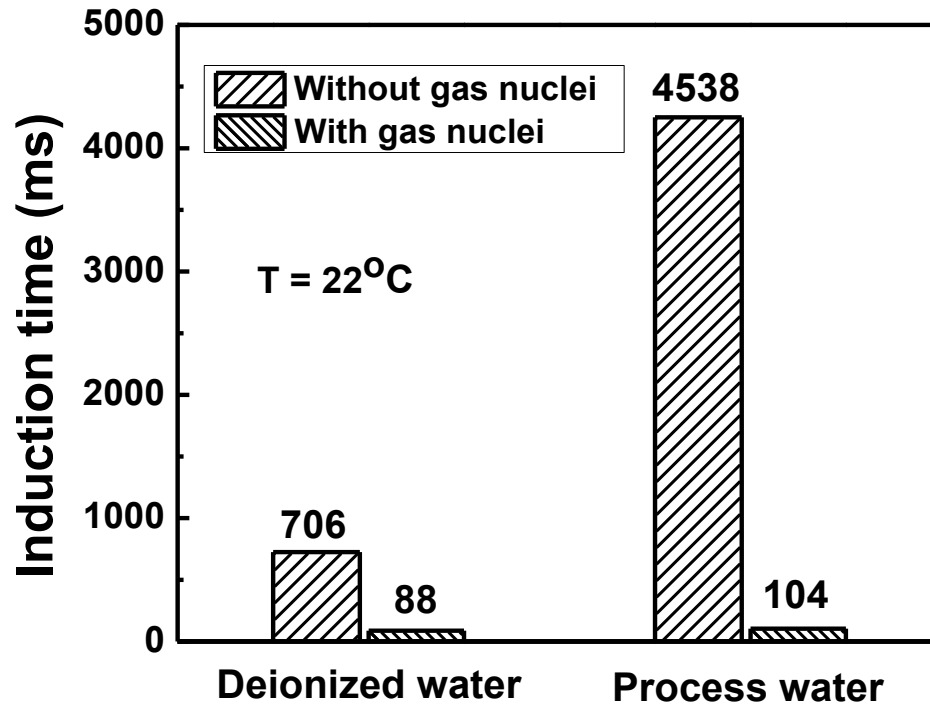


Figure 4-22. Induction time for silicon wafer ($\theta = 65^\circ$) with and without micron size bubbles in DI and Syncrude process water.

In the next investigation, flotation size bubbles were kept fresh, while the micron size bubbles were aged. In this way, the effect of aging the micron size bubbles only on the bubble/solid attachment can be investigated. Syncrude process water was used in the bubble aging tests. The experimental results are shown in Figure 4-23. It can be seen that aging the micron size bubbles for 20 minutes nearly doubled the induction time from 104 ms to 204 ms.

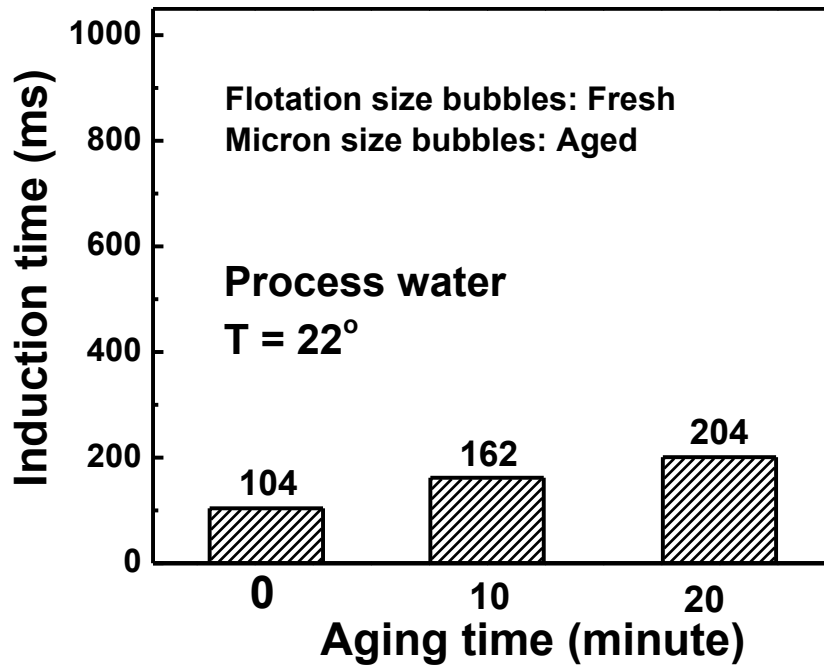


Figure 4-23. Effect of aging micron size bubbles on induction time.

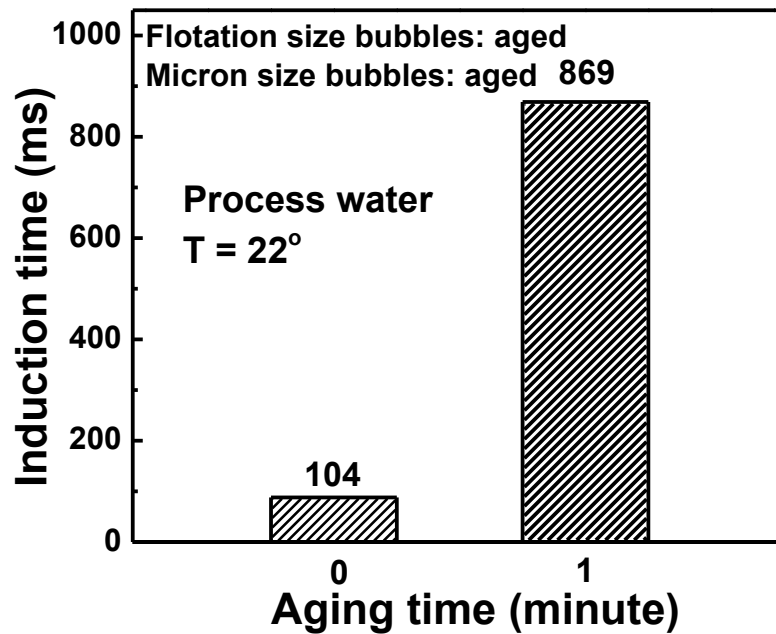


Figure 4-24. Effect of aging both flotation size and micron size bubbles on induction time. However, as shown in Figure 4-24, if both of the micron size and flotation size bubbles were aged simultaneously using Syncrude process water for just one minute, the induction

time increased greatly from 104 ms to 869 ms. The results show that bubble aging is detrimental to the bubble/particle attachment, especially when flotation size and micron size bubbles are aged simultaneously. Therefore, bubble aging is highly suggested to be avoided in flotation.

4.10 Heterogeneous nucleation

Wilt (1986) showed that the hydrophobicity of the solid surface, crevices on the surface, and gas saturation ratio affected the heterogeneous nucleation. Zhou et al. (2009) stated that heterogeneous nucleation might occur in the hydrodynamic cavitation assisted flotation. In this section, hydrodynamic cavitation on silicon wafers, galena and sphalerite surfaces was examined using the flow visualization cell. The effect of solid surface of hydrophobicity, crevices on the surface, and gas saturation on the heterogeneous nucleation was studied. The surface roughness of the silicon wafer was examined using atomic force microscopy (AFM). For most silicon wafers, surface roughness based on arithmetic mean was found to be less than 1 nm. However, a few crevices, which are referred to as natural crevices could be also found on the silicon wafer. The surface roughness of the galena and sphalerite surfaces polished using 1200/1600 grits sand paper was examined using confocal microscope (Zeiss 510). The results showed an arithmetic mean of the surface roughness to $1.6 \pm 0.25 \mu\text{m}$ and $1.1 \pm 0.18 \mu\text{m}$ for galena and sphalerite, respectively. To intentionally introduce crevices on the silicon, galena and sphalerite surfaces, the surfaces were scratched using 220 grits sand paper. The solid surfaces scratched by 220 grits sand paper are referred to as sand paper (220) in the report. The optical micrographs of galena and sphalerite surfaces polished by 220 grits sand paper are shown in Figure 4-25.

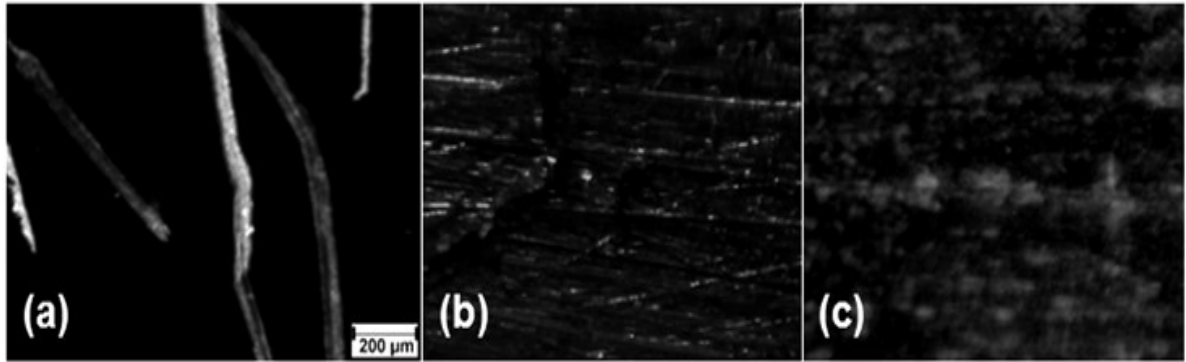


Figure 4-25. Optical micrographs of (a) silicon; (b) galena; (c) sphalerite surfaces after scratching with 220 grits sand paper.

The experiments for heterogeneous nucleation were repeated five more times. The experimental results are summarized in Table 2. Star (*) stands for no heterogeneous nucleation observed, the check mark (√) stands for extensive heterogeneous nucleation always observed, and VF (very few) stands for variable heterogeneous nucleation occasionally observed. The results in Table 2 show that the heterogeneous nucleation occurred at the locations of crevices on the solid surface.

To illustrate the evolution of heterogeneous nucleation, the sequences of heterogeneous nucleation on silicon wafer of contact angle equal to 96° at throat velocity of 6 m/s were captured and shown in Figure 4-26. From Figure 4-26 (a) to (d), we see the growth of gas cavity bubble at a crevice to greater than $100\ \mu\text{m}$, after which it was washed away by the flow fluid and a new gas cavity bubble formed as shown in Figure 4-26 (e). The natural crevice on the silicon wafer was shown to function as the nucleation site for the heterogeneous nucleation.

Table 2. Summary on observation of heterogeneous nucleation.

| Wafer material | Roughness | V_{throat} (m/s) | Solution | Contact angle ($^{\circ}$) | Heterogeneous nucleation |
|----------------|------------------|--------------------|-------------------------|------------------------------|--------------------------|
| Silicon | < 1nm | <13 | DI | ≤ 96 | x |
| Silicon | < 1nm | <13 | 700 ppm CO ₂ | ≤ 96 | x |
| Silicon | Nature crevice | 4-13 | DI | < 87 | x |
| Silicon | Nature crevice | 4-13 | DI | 96 | √ |
| Silicon | Nature crevice | < 4 | DI | 96 | x |
| Silicon | sand paper (220) | <4 | DI | < 87 | x |
| Silicon | sand paper (220) | 1-13 | 700 ppm CO ₂ | 96 | √ |
| Silicon | sand paper (220) | 4-13 | DI | 96 | √ |
| Silicon | sand paper (220) | <4 | DI | 96 | x |
| Galena | sand paper (220) | 5-13 | DI | 72-83 | VF |
| Galena | sand paper (220) | 5-13 | 700 ppm CO ₂ | 62-83 | √ |
| Galena | sand paper (220) | 5-13 | 700 ppm CO ₂ | <62 | x |
| Sphalerite | Sand paper (220) | 5-13 | DI | 72-87 | VF |
| Sphalerite | Sand paper (220) | 5-13 | 700 ppm CO ₂ | 72-87 | VF |
| Sphalerite | Sand paper (220) | 5-13 | 700 ppm CO ₂ | <72 | x |

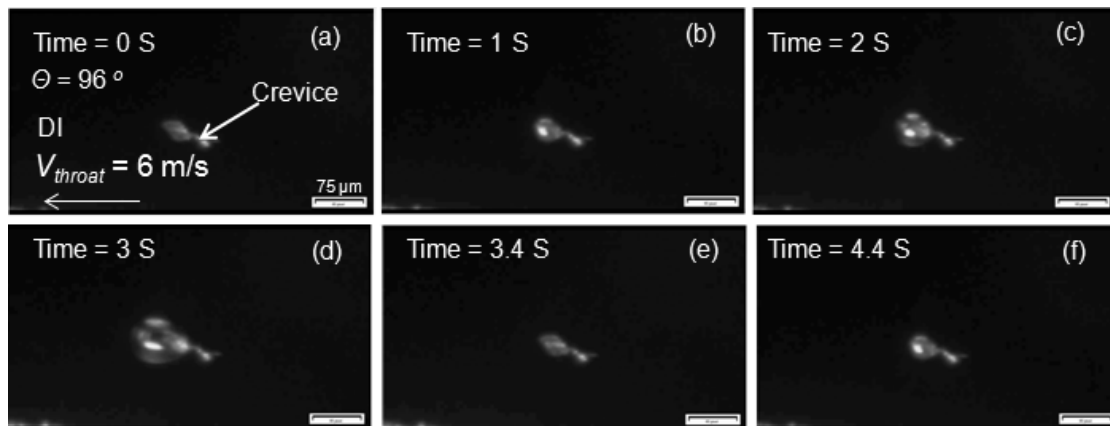


Figure 4-26. Heterogeneous nucleation on a silicon wafer of contact angle 96° in DI water at throat velocity of 6 m/s

The necessity of the crevices for heterogeneous nucleation is reported in previous studies. Wilt (1986) reported that minimum Gibbs free energy for gas nucleation, ΔG^* reduced when occurred at crevices, predicting that the crevices might be the nucleation sites for the heterogeneous nucleation. Ryan and Hemmingsen (1993) reported that very few bubbles could form on smooth surface in solution saturated with N_2 at saturation pressure up to 125 atm. However, when rough surface was used, extensive heterogeneous nucleation was observed at saturation pressure of N_2 as low as 10 to 15 atm. Ryan and Hemmingsen (1993) confirmed that heterogeneous nucleation formed only on the hydrophobic surface. In addition to crevices and hydrophobicity, our experimental results also show that increasing the dissolved gas content by CO_2 saturation is an effective way to enhance the heterogeneous nucleation, which is in line with the impact of reducing ΔG^* . From our study, we can assume that heterogeneous nucleation most likely takes place on the crevices of the hydrophobic coal particles in flotation. Therefore, grinding process which creates extensive crevices would enhance the heterogeneous nucleation and hence fine particle flotation. One shortcoming in present study is that the shape of the crevices on the solid surface was not well controlled. According to Wilt (1986), the shape of the crevices could affect the generation rate of heterogeneous nucleation significantly. Therefore, controlling the shape of crevices is considered as an important factor, which is worth further study to determine the accurate criteria of the heterogeneous nucleation.

Chapter 5

Conclusions

In this study, homogeneous and heterogeneous gas nucleation induced by hydrodynamic cavitation was investigated. The effect of the fluid velocity, dissolved gas content and the addition of frother on the size and the number counts of bubbles in homogeneous nucleation were determined. The interaction between fine coal and micron size bubbles was studied using a model system. The effect of fluid velocity, dissolved gas content, solid concentration, particle hydrophobicity, external air entrainment on fine particle aggregation was examined. The effect of the presence of micron size bubbles and bubble aging on the bubble\particle interaction was also examined. Finally, heterogeneous nucleation on solid surfaces of varying hydrophobicity and surface roughness was shown. The following conclusions were made based on experimental results:

- For homogeneous nucleation, micron size bubbles with D_{c32} of 30 μm to 40 μm were observed as long as the throat velocity exceeded 8 m/s. Further increasing fluid velocity, dissolved gas content, and addition of frother had little effect on the size of micron size bubbles but increased the number counts of bubbles generated.
- For the model flotation system, micron size bubbles did not attach to the surface or fine particles of contact angle less than 45° . Increasing throat velocity and dissolved gas content increased the recovery of hydrophobic fine coal. Finally, injecting an appropriate amount external air benefited the recovery of hydrophobic fine coal. However, excessive air injection resulted in the blockages of cavitation tube by air, which was detrimental to the recovery of hydrophobic fine coal.

- The induction time measurement proved that the presence of micron size bubbles on the solid surfaces greatly enhanced the attachment between flotation size bubbles and solid surfaces. Additionally, the attachment between flotation size bubbles and solid surfaces decreased when micron size and flotation size bubbles were aged.
- The preliminary heterogeneous nucleation investigation showed that the nucleation took place only on the crevices on hydrophobic surfaces. Increasing throat velocity and dissolved gas content enhanced heterogeneous nucleation.

In this study, the qualitative criteria for the hydrodynamic cavitation in bulk solution and on solid surface were established. A model system was designed to clarify the interaction between micron size bubbles generated by hydrodynamic cavitation and fine particles under various conditions. The results are beneficial to the design of specific bubble generator for fine particle flotation.

Chapter 6

Future Work

Through this study, the mechanisms regarding the generation of micron size bubbles and the interaction between fine particles and micron size bubbles have been further advanced. However, continuous efforts are required to realize and maximize hydrodynamic cavitation in fine particle flotation.

From this study, a two-stage aeration concept has been proposed. To realize this two-stage aeration concept, the design and fabrication of a dual bubble generator (a bubble generator combining of both micron size and flotation size bubbles) should be carefully considered in near future. Considering that aging of both micron size and flotation size bubbles is detrimental to the bubble/solid attachment, the design of the dual generator should emphasize the close proximity of generating micron size and flotation size bubbles.

Further experiments should be conducted to investigate the effect of hydrodynamic cavitation on flotation selectivity. It is important to establish the optimum operation parameters for the two-stage aeration for a flotation column.

References

- Anfruns, J. F. and J. A. Kitchener (1977). "Rates of capture of small particles in flotation." Transactions of the Institution of Mining and Metallurgy, Section C: Mineral Processing and Extractive Metallurgy **86**: c9-c15.
- Athavale, M. M., H. Y. Li, Y. U. Jiang and A. K. Singhal (2002). "Application of the full cavitation model to pumps and inducers." International Journal of Rotating Machinery **8**(1): 45-56.
- Becker, P. J., F. Puel, Y. Chevalier and N. Sheibat-Othman (2014). "Monitoring silicone oil droplets during emulsification in stirred vessel: Effect of dispersed phase concentration and viscosity." Canadian Journal of Chemical Engineering **92**(2): 296-306.
- Berahman, B. (2012). "A Preliminary Study on Pyrolysis and Gasification of haltenes and Coal-Asphaltenes Slurry in Entrained Flow." University of Alberta, Edmonton. **Master of Science.**
- Blake F. G. (1949). "Onset of Cavitation in Liquids." Harvard University, Cambridge. **Doctor of Philosophy.**
- Borkent, B., N. Bremond, M. Arora, C. D. Ohl and D. Lohse (2008). "Is there gas entrapped on submerged silicon wafers? Visualizing nano-scale bubbles with cavitation." Solid State Phenomena **134**: 225-228.
- Boström, M., V. Deniz, G. V. Franks and B. W. Ninham (2006). "Extended DLVO theory: Electrostatic and non-electrostatic forces in oxide suspensions." Advances in Colloid and Interface Science **123–126**(0): 5-15.
- Brennen, C.E. (1995). "Cavitation and Bubble Dynamics." Oxford University Press, New York.

- Chen, F., C. O. Gomez and J. A. Finch (2001). "Technical note bubble size measurement in flotation machines." Minerals Engineering **14**(4): 427-432.
- Clift R., G. J. R., Weber M. (2005). "Bubble, Particle, and Drops." New York, Dover Publications.
- Collins, D. N. and A. D. Read (1971). "Treatment of slimes." Miner Sci Eng **3**(2): 19-31.
- Crawford, R. and J. Ralston (1988). "The influence of particle size and contact angle in mineral flotation." International Journal of Mineral Processing **23**(1-2): 1-24.
- Derjaguin, B. V. and S. S. Dukhin (1993). "Theory of flotation of small and medium-size particles." Progress in Surface Science **43**(1-4): 241-266.
- Dianzuo, W., Q. Guanzhou and H. Weibal (1988). "The effect of carrier-promoting aggregation of coarse particles." Fine Particle Flotation: 309-316.
- Ding, P., M. G. Orwa and A. W. Pacek (2009). "De-agglomeration of hydrophobic and hydrophilic silica nano-powders in a high shear mixer." Powder Technology **195**(3): 221-226.
- Du, H. and J. D. Miller (2007). "A molecular dynamics simulation study of water structure and adsorption states at talc surfaces." International Journal of Mineral Processing **84**(1-4): 172-184.
- ERIEZ. (2013). "CPT cavitation system."
<http://efd.eriez.com/products/index/cavitationtube>
- Feng, D. and C. Aldrich (1999). "Effect of particle size on flotation performance of complex sulphide ores." Minerals Engineering **12**(7): 721-731.

- Féris, L. A., C. W. Gallina, R. T. Rodrigues and J. Rubio (2001). "Optimizing dissolved air flotation design and saturation." Water Science & Technology **43**: 145-152.
- Fletcher, N. H. (1959). "Erratum: Size effect in heterogeneous nucleation." The Journal of Chemical Physics **31**(4): 1136-1137.
- Finch, J. A. and C. A. Hardie (1999). "Example of innovation from the waste management industry: Deinking flotation cells." Minerals Engineering **12**(5): 467-475.
- Finch, J. A., J. E. Nasset and C. Acuña (2008). "Role of frother on bubble production and behaviour in flotation." Minerals Engineering **21**(12-14): 949-957.
- Jamialahmadi, M., C. Branch and H. Muller-Steinhagen (1994). "Terminal bubble rise velocity in liquids." Chemical Engineering Research and Design **72**(A1): 119-122.
- Gorain, B. K., J. P. Franzidis and E. V. Manlapig (1997). "Studies on impeller type, impeller speed and air flow rate in an industrial scale flotation cell. Part 4: Effect of bubble surface area flux on flotation performance." Minerals Engineering **10**(4): 367-379.
- Gu, G., Z. Xu, K. Nandakumar and J. Masliyah (2003). "Effects of physical environment on induction time of air-bitumen attachment." International Journal of Mineral Processing **69**(1-4): 235-250.
- Grau, R. A. and K. Heiskanen (2003). "Gas dispersion measurements in a flotation cell." Minerals Engineering **16**(11): 1081-1089.
- Harvey, E. N., W. D. McElroy and A. H. Whiteley (1947). "On cavity formation in water." Journal of Applied Physics **18**(2): 162-172.

- Hemmingsen, E. A. (1975). "Cavitation in gas-supersaturated solutions." Journal of Applied Physics **46**(1): 213-218.
- Hu, H., Z. Zhou, Z. Xu and J. A. Finch (1998). "Numerical and experimental study of a hydrodynamic cavitation tube." Metallurgical and Materials Transactions B: Process Metallurgy and Materials Processing Science **29**(4): 911-917.
- Jamialahmadi, M., C. Branch and H. Muller-Steinhagen (1994). "Terminal bubble rise velocity in liquids." Chemical Engineering Research and Design **72**(A1): 119-122.
- Kail, N., H. Briesen and W. Marquardt (2008). "Analysis of FBRM measurements by means of a 3D optical model." Powder Technology **185**(3): 211-222.
- Kail, N., W. Marquardt and H. Briesen (2009). "Process analysis by means of focused beam reflectance measurements." Industrial and Engineering Chemistry Research **48**(6): 2936-2946.
- Keller, A. P. (2001). "Cavitation scale effects-empirically found relations and the correlation of Cavitation Number and Hydrodynamic Coefficients." <http://resolver.caltech.edu/cav2001:lecture.001>.
- Koh, P. T. L., F. P. Hao, L. K. Smith, T. T. Chau and W. J. Bruckard (2009). "The effect of particle shape and hydrophobicity in flotation." International Journal of Mineral Processing **93**(2): 128-134.
- Kumar, V., M. K. Taylor, A. Mehrotra and W. C. Stagner (2013). "Real-time particle size analysis using focused beam reflectance measurement as a process analytical technology tool for a continuous granulation-drying-milling process." AAPS PharmSciTech **14**(2): 523-530.

- Laskowski, J. (2001). "Coal Flotation and Fine Coal Utilization." Gulf Professional Publishing.
- Lazaridis, N. K., K. A. Matis, G. A. Stalidis and P. Mavros (1992). "Dissolved-air flotation of metal ions." Separation Science and Technology **27**(13): 1743-1758.
- Lee, S. Y. and Y. D. Choi (2003). "Turbulence generation by ultrasonically induced gaseous cavitation in the CO₂ saturated water flow." KSME International Journal **17**(8): 1203-1210.
- Lu, S., Y. Ding and J. Guo (1998). "Kinetics of fine particle aggregation in turbulence." Advances in Colloid and Interface Science **78**(3): 197-235.
- Motarjemi, M. and G. J. Jameson (1978). "Mass transfer from very small bubbles—the optimum bubble size for aeration." Chemical Engineering Science **33**(11): 1415-1423.
- Melo F., (2001). "Fundamental Properties of Flotation Frothers and Their Effect on Flotation. Mining Engineering." University of British Columbia, Vancouver. **Master of Applied Science.**
- Nesset, J. E., J. R. Hernandez-Aguilar, C. Acuna, C. O. Gomez and J. A. Finch (2006). "Some gas dispersion characteristics of mechanical flotation machines." Minerals Engineering **19**(6-8): 807-815.
- Noppel, M., H. Vehkamäki, P. M. Winkler, M. Kulmala and P. E. Wagner (2013). "Heterogeneous nucleation in multi-component vapor on a partially wettable charged conducting particle. II. the generalized Laplace, Gibbs-Kelvin, and Young equations and application to nucleation." Journal of Chemical Physics **139**(13).

- Oliveira, R. C. G., G. Gonzalez and J. F. Oliveira (1999). "Interfacial studies on dissolved gas flotation of oil droplets for water purification." Colloids and Surfaces A: Physicochemical and Engineering Aspects **154**(1-2): 127-135.
- Parker, J. L., P. M. Claesson and P. Attard (1994). "Bubbles, cavities, and the long-ranged attraction between hydrophobic surfaces." Journal of Physical Chemistry **98**(34): 8468-8480.
- Parkinson, L. and J. Ralston (2011). "Dynamic aspects of small bubble and hydrophilic solid encounters." Advances in Colloid and Interface Science **168**(1-2): 198-209.
- Pawlik, M., J. S. Laskowski and F. Melo (2004). "Effect of coal surface wettability on aggregation of fine coal particles." Coal Preparation **24**(5-6): 233-248.
- Piñeres, J. and J. Barraza (2011). "Energy barrier of aggregates coal particle–bubble through the extended DLVO theory." International Journal of Mineral Processing **100**(1–2): 14-20.
- Ponasse, M., V. Dupre, Y. Aurelle and A. Secq (1998). "Bubble formation by water release in nozzle - II. Influence of various parameters on bubble size." Water Research **32**(8): 2498-2506.
- Qian, M. and J. Ma (2009). "Heterogeneous nucleation on convex spherical substrate surfaces: A rigorous thermodynamic formulation of Fletcher's classical model and the new perspectives derived." Journal of Chemical Physics **130**(21): 214709.
- Randall, E. W., C. M. Goodall, P. M. Fairlamb, P. L. Dold and C. T. O'Connor (1989). "A method for measuring the sizes of bubbles in two- and three-phase systems." Journal of Physics E: Scientific Instruments **22**(10): 827-833.

- Rodrigues, R. T. and J. Rubio (2003). "New basis for measuring the size distribution of bubbles." Minerals Engineering **16**(8): 757-765.
- Rodrigues, R. T. and J. Rubio (2007). "DAF–dissolved air flotation: Potential applications in the mining and mineral processing industry." International Journal of Mineral Processing **82**(1): 1-13.
- Rooze, J., M. André, G.-J. van der Gulik, D. Fernández-Rivas, J. Gardeniers, E. Rebrov, J. Schouten and J. Keurentjes (2012). "Hydrodynamic cavitation in micro channels with channel sizes of 100 and 750 micrometers." Microfluidics and Nanofluidics **12**(1): 499-508.
- Ross, D., W. A. Kuperman (1989). "Mechanics of underwater noise." Acoustical Society of America **86**(4): 1626-1626.
- Ryan, W. L. and E. A. Hemmingsen (1993). "Bubble formation in water at smooth hydrophobic Surfaces." Journal of Colloid and Interface Science **157**(2): 312-317.
- Schäfer, R., C. Merten and G. Eigenberger (2002). "Bubble size distributions in a bubble column reactor under industrial conditions." Experimental Thermal and Fluid Science **26** (6–7): 595-604.
- Sear, R. P. (2006). "Heterogeneous and homogeneous nucleation compared: Rapid nucleation on microscopic impurities." Journal of Physical Chemistry B **110**(10): 4985-4989.
- Sigsbee, R. and G. Pound (1967). "Heterogeneous nucleation from the vapor." Advances in Colloid and Interface Science **1**(3): 335-390.

- Singhal, A. K., M. M. Athavale, H. Li and Y. Jiang (2002). "Mathematical basis and validation of the full cavitation model." Journal of Fluids Engineering **124** (3): 617-624.
- Sobhy, A. and D. Tao (2013). "High-efficiency nanobubble coal flotation." International Journal of Coal Preparation and Utilization **33**(5): 242-256.
- Song, S., Lopez-Valdivieso, A., Reyes-Bahena, J. L. (1999). "Hydrophobic flocculation applied to fine mineral and coal processing." In: XXIII Congress AIMMGM., Mexico p: 1-20.
- Song, S., A. Lopez-Valdivieso, J. L. Reyes-Bahena, H. I. Bermejo-Perez and O. Trass (2000). "Hydrophobic flocculation of galena fines in aqueous suspensions." Journal of Colloid and Interface Science **227** (2): 272-281.
- Song, S., A. Lopez-Valdivieso, J. L. Reyes-Bahena and C. Lara-Valenzuela (2001). "Floc flotation of galena and sphalerite fines." Minerals Engineering **14** (1): 87-98.
- Song, S., X. Zhang, B. Yang and A. Lopez-Mendoza (2012). "Flotation of molybdenite fines as hydrophobic agglomerates." Separation and Purification Technology **98**(0): 451-455.
- Subrahmanyam, T. V. and K. S. E. Forssberg (1990). "Fine particles processing: shear-flocculation and carrier flotation - a review." International Journal of Mineral Processing **30** (3-4): 265-286.
- Takahashi, T., T. Miyahara and H. Mochizuki (1979). "Fundamental study of bubble formation in dissolved air pressure flotation." Journal of Chemical Engineering of Japan **12**(4): 275-280.

- Tao, D. (2004). "Role of bubble size in flotation of coarse and fine particles - a review." Separation Science and Technology **39**(4): 741-760.
- Tao, D., S. Yu, X. Zhou, R. Q. Honaker and B. K. Parekh (2008). "Picobubble column flotation of fine coal." International Journal of Coal Preparation and Utilization **28**(1): 1-14.
- Tao, Y., J. Liu, S. Yu and D. Tao (2006). "Picobubble enhanced fine coal flotation." Separation Science and Technology **41**(16): 3597-3607.
- Taylor, C., J. A. Johnson and W. R. Smith, Eds. (1983). "Numerical methods in laminar and turbulent flow." International Journal of Heat and Fluid Flow **4**(4): 228.
- Toxvaerd, S. (2002). "Molecular dynamics simulation of heterogeneous nucleation at a structureless solid surface." Journal of Chemical Physics **117**(22): 10303-10310.
- Trahar, W. J. and L. J. Warren (1976). "The flotability of very fine particles — A review." International Journal of Mineral Processing **3**(2): 103-131.
- Tucker, J. P., D. A. Deglon, J. P. Franzidis, M. C. Harris and C. T. O'Connor (1994). "An evaluation of a direct method of bubble size distribution measurement in a laboratory batch flotation cell." Minerals Engineering **7**(5-6): 667-680.
- Wang, L. and R. H. Yoon (2008). "Effects of film elasticity and surface forces on the stability of foams and lamellae films in the presence of non-ionic surfactants. " THE XV INTERNATIONAL CONGRESS ON RHEOLOGY: The Society of Rheology 80th Annual Meeting **1027**(1): 839-841.
- Wang L. (2013). "A study of interactions between an air bubble and a solid surface in liquid." University of Alberta, Edmonton, Dissertation for **Doctor of Philosophy**.

- Warren, L. J. (1975). "Shear-flocculation of ultrafine scheelite in sodium oleate solutions." Journal of Colloid and Interface Science **50**(2): 307-318.
- Wei, S., D. Meijiao and H. Yuehua (2009). "Fine particle aggregation and flotation behavior induced by high intensity conditioning of a CO₂ saturation slurry." Mining Science and Technology **19**(4): 483-488.
- Wilt, P. M. (1986). "Nucleation rates and bubble stability in water-carbon dioxide solutions." Journal of Colloid and Interface Science **112**(2): 530-538.
- Witharana, S., B. Phillips, S. Strobel, H. D. Kim, T. McKrell, J. B. Chang, J. Buongiorno, K. K. Berggren, L. Chen and Y. Ding (2012). "Bubble nucleation on nano- to micro-size cavities and posts: An experimental validation of classical theory." Journal of Applied Physics **112**(6): 064904.
- Wu, C. (2011). "A fundamental study of bubble-particle interaction through zeta-potential distribution analysis. Department of Chemical and Materials Engineering." University of Alberta, Edmonton, Thesis for **Master of Science**.
- Wu, C., K. Nasset, J. Masliyah and Z. Xu (2012). "Generation and characterization of submicron size bubbles." Advances in Colloid and Interface Science **179**:121-132.
- Xu, Q., Nakajima, M., Ichikawa, S., Nakamura, N., Shiina T. (2008). "A comparative study of microbubble generation by mechanical agitation and sonication." Innovative Food Science and Emerging Technologies. **9**(4), 489-494.
- Xu, Z. and R.-H. Yoon (1989). "The role of hydrophobia interactions in coagulation." Journal of Colloid and Interface Science **132**(2): 532-541.

- Xu, Z. and R. H. Yoon (1989). "The role of hydrophobia interactions in coagulation." Journal of Colloid and Interface Science **132**(2): 532-541.
- Xu, Z. (2000). "Flotation historical development." Encyclopedia of Separation Science: 1527-1537.
- Yap, N., D. Feng, R. R. Dagastine, G. C. Lukey and J. S. J. Van Deventer (2005). "Direct force measurement between an irregular particle and an air bubble." Current Opinion in Colloid & Interface Science **6**(4), 383-401
- Yoon, R.-H., D. H. Flinn and Y. I. Rabinovich (1997). "Hydrophobic interactions between dissimilar surfaces." Journal of Colloid and Interface Science **185**(2): 363-370.
- Yoon, R. H. (1993). "Microbubble Flotation." Minerals Engineering **6**(6): 619-630.
- Yoon, R. H. and G. H. Luttrell (1986). "The effect of bubble size on fine coal flotation." Coal Preparation **2**(3): 179-192.
- Yu, S., R. Honaker, D. Tao and B. K. Parekh (2006). "Picobubble enhanced column flotation of fine coal." International Journal of Coal Preparation and Utilization **28**(1),:1-14.
- Zhang, W. and D. Z. Zhu (2013). "Bubble characteristics of air–water bubbly jets in crossflow." International Journal of Multiphase Flow **55**(0): 156-171.
- Zhou, Z. a. (1996). "Gas nucleation and cavitation in flotation." McGill University, Montreal, **Doctor of Philosophy**.
- Zhou, Z. A., R. S. Chow, P. Cleyle, Z. H. Xu and J. H. Masliyah (2010). "Effect of dynamic bubble nucleation on bitumen flotation." Canadian Metallurgical Quarterly **49**(4): 363-372.

- Zhou, Z. A., R. Langlois, Z. Xu and J. A. Finch (1997). "In plant testing of a hydrodynamic cavitation reactor in flotation." Mineral Processing and Environment **51**(1), 139-149.
- Zhou, Z. A., H. Li, R. Chow and K. Roberge (2013). "Role of carrier flotation in accelerating bitumen extraction recovery from mineable athabasca oil sands." The Canadian Journal of Chemical Engineering **91**(8): 1340-1348.
- Zhou, Z. A., Z. Xu, J. A. Finch, H. Hu and S. R. Rao (1997). "Role of hydrodynamic cavitation in fine particle flotation." International Journal of Mineral Processing **51**(1-4): 139-149.
- Zhou, Z. A., Z. Xu, J. A. Finch, J. H. Masliyah and R. S. Chow (2009). "On the role of cavitation in particle collection in flotation - A critical review. II." Minerals Engineering **22**(5): 419-433.

Appendix A: Bubble Size Correction for Image Analysis

As shown in Figure AI-1, bubbles deformed when they attached to the silicon substrate. The actual bubble size is the diameter of bubbles in the solution. However, the diameter on the images captured by the microscope is the diameter of the projection of bubbles on the silicon substrate.

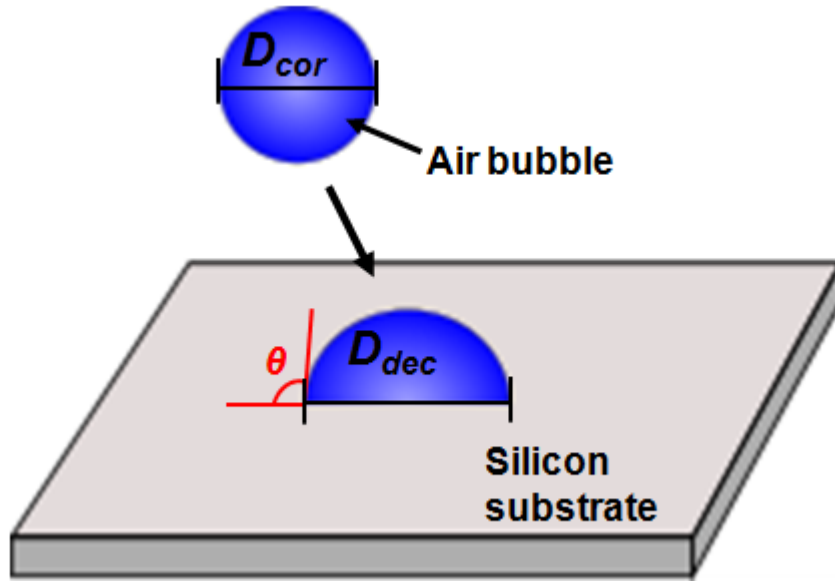


Figure AI-1. The illustration of the deformation of the bubbles when the bubbles in the solution attached to the substrate.

In the following, the correction process used to transfer the diameter from the images (D_{dec}) to the actual bubble size (D_{cor}) is demonstrated. Since the volume of bubble before and after attachment is same, following relationship can be derived:

$$\left\{ \frac{2\pi}{3 \sin(\pi - \theta)^3} [1 - \cos(\pi - \theta)] - \frac{\pi \cos(\pi - \theta)}{3 \sin(\pi - \theta)} \right\} \frac{1}{8} D_{dec}^3 = \frac{\pi}{6} D_{cor}^3 \quad (AI-1)$$

where the D_{dec} is the detected bubble diameter; D_{cor} is the bubble diameter after correction; θ is the contact angle of the silicon substrate. By arranging the equation AI-1, we can obtain:

$$D_{cor} = \alpha_{cor} D_{dec} \quad (\text{AI-2})$$

$$\alpha_{cor} = \frac{\left(\frac{1}{2} - \cos(\pi - \theta) - \frac{1}{4} \sin(\pi - \theta)^2 \cos(\pi - \theta) \right)^{\frac{1}{3}}}{\sin(\pi - \theta)} \quad (\text{AI-3})$$

The contact angle (θ) of the substrate is 96° , so the calculated is 0.767.